Phospho-regulated auto-inhibition of Cnn controls microtubule nucleation during cell division

Corinne A. Tovey[1,2], Chisato Tsuji[1], Alice Egerton[1], Fred Bernard[2], Antoine Guichet[2], Marc de la Roche[3], Paul T. Conduit[1, 2, 4]

[1]Department of Zoology, University of Cambridge, Downing Street, Cambridge, CB2 3EJ

[2]Université de Paris, CNRS, Institut Jacques Monod, F75006, Paris, France.

[3]Department of Biochemistry, University of Cambridge, 80 Tennis Court Road, Cambridge, CB2 1GA, United Kingdom

[4]Corresponding author
Paul T. Conduit
0033 (1) 57 27 80 95
Paul.conduit@ijm.fr

Abstract

γ-tubulin-ring-complexes (γ-TuRCs) nucleate microtubules. They are recruited to centrosomes in dividing cells via binding to N-terminal CM1 domains within γ-TuRC-tethering proteins, including *Drosophila* Cnn. Binding promotes microtubule nucleation and is restricted to centrosomes, but the mechanism regulating binding remains unknown. Here we identify an extreme N-terminal "CM1 auto-inhibition" (CAI) domain within the centrosomal isoform of Cnn (Cnn-C) that inhibits γ-TuRC binding. Cnn-C is phosphorylated at centrosomes and we find that phospho-mimicking sites within the CAI domain helps relieve auto-inhibition. In contrast, the testes-specific mitochondrial Cnn-T isoform lacks the CAI domain and can bind strongly to cytosolic γ-TuRCs. Ubiquitously expressing a version of Cnn-C lacking the CAI domain leads to major cell division defects, which appears to be due to ectopic cytosolic microtubule nucleation. We propose that the CAI domain folds back to sterically inhibit the CM1 domain, and that this auto-inhibition is relieved by phosphorylation that occurs specifically at centrosomes.

Introduction

Microtubules are polarised polymers of tubulin necessary for cell function (Akhmanova and Steinmetz, 2015). They provide structural support, pulling and pushing forces, and tracks for the transport of intracellular cargo. Microtubules are arranged into specialised arrays that are crucial for cell function, such as the mitotic spindle or the polarised arrays within neurons. Correct assembly of these arrays relies in part on the spatiotemporal regulation of microtubule formation, and this is achieved by restricting microtubule formation and organisation to specific microtubule organising centres (MTOCs), such as the centrosome during mitosis or Golgi apparatus in motile fibroblasts (Tillery et al., 2018; Sanchez and Feldman, 2016; Petry and Vale, 2015).

The common link between most MTOCs is the presence of multi-protein γ-tubulin ring complexes (γ-TuRCs) (Teixidó-Travesa et al., 2012; Tovey and Conduit, 2018; Lin et al., 2014a; Farache et al., 2018), which template and catalyse the kinetically unfavourable process of microtubule nucleation (Kollman et al., 2011). γ-TuRCs are recruited to MTOCs by γ-TuRC-tethering proteins, that directly link γ-TuRCs to the MTOC (Tovey and Conduit, 2018). γ-TuRCs contain 14 γ-tubulin molecules held in a single-turn helical shape by laterally associating γ-tubulin complex proteins (GCPs) (Kollman et al., 2011). The γ-tubulin molecules bind directly to α/β-tubulin dimers to promote new microtubule assembly (Thawani et al., 2020). γ-TuRCs have a low activity within the cytosol but are thought to be “activated” after recruitment to MTOCs (Tovey and Conduit, 2018; Farache et al., 2018). In this model, the controlled recruitment and activation of γ-TuRCs enables the spatiotemporal control of microtubule nucleation and array formation. Consistent with this model, recent structural studies have shown that γ-TuRCs purified from the cytosol of HeLa cells and *Xenopus* eggs are in a semi-open conformation, in which the γ-tubulin molecules do not perfectly match the geometry of a 13 protofilament microtubule (Consolati et al., 2020; Liu et al., 2019; Wieczorek et al., 2019). A conformational change into a fully closed ring that perfectly matches the geometry of a microtubule is expected to increase the nucleation capacity of the γ-TuRC (Liu et al., 2019; Consolati et al., 2020). This agrees with studies in budding yeast, where a conformational change is observed and artificial closure of the ring increases microtubule nucleation capacity (Kollman et al., 2015).

How activation via an open-to-closed conformation change occurs is currently unclear, but various factors have been reported to increase the capacity for γ-TuRCs to nucleate microtubules. The nucleation capacity of γ-TuRCs purified from *Xenopus* egg extract is

67 dramatically increased by the addition of the TOG domain protein XMAP215 (Thawani et al.,
68 2020). TOG domain family members mediate α/β-tubulin addition via their TOG domains
69 (Nithianantham et al., 2018), bind directly to γ-tubulin, and function in microtubule nucleation
70 *in vivo* (Thawani et al., 2018; Flor-Parra et al., 2018; Gunzelmann et al., 2018). Single
71 molecule experiments combined with modelling suggest that XMAP215 indirectly promotes
72 the open-to-closed conformation change of purified γ-TuRCs by increasing the chance of
73 protofilament formation, where the lateral contacts between protofilaments are predicted to
74 force the closure of the γ-TuRC (Thawani et al., 2020). While this is an attractive model,
75 evidence suggests that γ-TuRC activation can occur in different ways and may be context
76 specific. Phosphorylation of γ-TuRCs by Aurora A around mitotic chromatin increases the
77 activity of γ-TuRCs (Scrofani et al., 2015; Pinyol et al., 2013), as does the addition of NME7
78 kinase *in vitro* (Liu et al., 2014). γ-TuRC activity is also increased after binding of the Augmin
79 complex (Tariq et al., 2020), which occurs on the side of pre-existing microtubules such as
80 within the mitotic spindle (Goshima et al., 2008; Uehara et al., 2009; Zhu et al., 2008; Lawo et
81 al., 2009). Another potential γ-TuRC activator is the Centrosomin Motif 1 (CM1) domain, which
82 is conserved in γ-TuRC-tethering proteins across Eukaryotes (Sawin et al., 2004; Lin et al.,
83 2014b). Addition of protein fragments containing part of the CM1 domain, known as γ-TuNA,
84 dramatically increases the nucleation capacity of γ-TuRCs purified from human cells (Choi et
85 al., 2010; Muroyama et al., 2016), although the degree of this activity change is much lower
86 when using γ-TuRCs purified from *Xenopus* eggs (Liu et al., 2019; Thawani et al., 2020). While
87 there is evidence that CM1-domain binding does not alter the semi-open conformation of
88 purified γ-TuRCs (Wieczorek et al., 2019; Liu et al., 2019), expression of γ-TuNA within human
89 cells leads to the ectopic nucleation of microtubules throughout the cytosol, and this effect is
90 abolished by the introduction of mutations that prevent CM1 domain binding to γ-TuRCs or by
91 the depletion of γ-TuRC components (Choi et al., 2010; Hanafusa et al., 2015; Cota et al.,
92 2017). Similar effects are seen in fission yeast, where expression of fragments of Mto1
93 containing the CM1 domain results in cytosolic microtubule nucleation (Lynch et al., 2014),
94 and in *Xenopus* egg extracts containing activated Ran which, when supplemented with CM1-
95 domain fragments, show dramatically increased random microtubule aster formation (Liu et
96 al., 2019). Thus, while CM1-domain binding may not directly alter γ-TuRC conformation *in*
97 *vitro*, there is strong evidence that it induces an activity change in various contexts *in vivo*.
98
99 Given that CM1-domain binding appears to increase γ-TuRC activity, this binding must be
100 spatiotemporally controlled under normal conditions. Indeed, results from numerous mass
101 spectrometry experiments on purified γ-TuRCs have shown that γ-TuRCs do not associate

102 with CM1-domain proteins within the cytosol (Choi et al., 2010; Oegema et al., 1999; Hutchins
103 et al., 2010; Teixidó-Travesa et al., 2012; Thawani et al., 2018; Consolati et al., 2019; Liu et
104 al., 2019; Wieczorek et al., 2019). Rather, CM1 domain proteins are thought to bind γ-TuRCs
105 only at MTOCs, such as the centrosome during mitosis. This presumably helps to ensure that
106 γ-TuRCs do not become active within the cytosol, but how CM1-domain binding is controlled
107 still remains unknown.
108
109 In this paper, we investigate how the binding between the *Drosophila* CM1-domain protein
110 Centrosomin (Cnn) and γ-TuRCs is regulated. Cnn is the only CM1-domain protein in
111 *Drosophila* but is a multi-isoform gene with all isoforms containing the CM1 domain (Eisman
112 et al., 2009). The centrosomal isoform (Cnn-C) has a dual role, both in recruiting γ-TuRCs to
113 centrosomes (Zhang and Megraw, 2007; Conduit et al., 2014b) and in forming a centrosome-
114 scaffold that supports mitotic PCM assembly (Conduit et al., 2014a; Feng et al., 2017).
115 Phosphorylation of a central PReM domain by Polo kinase drives the oligomerisation of Cnn-
116 C molecules via interactions between the PReM and C-terminal CM2 domain to promote
117 formation of the centrosome-like scaffold, and this occurs specifically at centrosomes (Conduit
118 et al., 2014a; Feng et al., 2017). A testes-specific Cnn-T isoform, which has mitochondrial
119 localisation domains instead of the PReM and CM2 domains, recruits γ-TuRCs to
120 mitochondria in sperm cells (Chen et al., 2017). Cnn-T also has a different, shorter, N-terminal
121 region upstream of the CM1 domain. We previously showed that N-terminal fragments of Cnn-
122 T could immunoprecipitate γ-TuRCs more readily than the equivalent fragments of Cnn-C
123 (Tovey et al., 2018). Here we confirm this result using an *in vivo* recruitment assay and show
124 that the failure of Cnn-C to bind γ-TuRCs is due to the N-terminal extension region absent
125 from Cnn-T. Truncating this N-terminal extension allows Cnn-C to bind γ-TuRCs, as does the
126 introduction of phospho-mimetic mutations into a conserved α-helix within the N-terminal
127 extension. Mimicking just one of these sites, a conserved Polo kinase site, also increases
128 binding, suggesting that Polo kinase regulates Cnn-C-to-γ-TuRC binding as well as Cnn-C
129 scaffolding. Collectively, our data suggests that centrosome-specific phosphorylation of Cnn-
130 C's N-terminal extension by Polo kinase helps relieve Cnn-C auto-inhibition to ensure γ-TuRC
131 binding specifically at centrosomes. This regulation is important, as expression of a modified
132 form of Cnn-C, where the auto-inhibited N-terminal region of Cnn-C was exchanged for the
133 unregulated γ-TuRC-binding N-terminal region of Cnn-T, results in major cell division defects,
134 apparently caused by ectopic cytosolic microtubule nucleation.

135 # Results

136 **The N-terminal regions of Cnn isoforms differ in their ability to bind γ-TuRCs**

137 We previously published evidence that different isoforms of Cnn bind γ-TuRCs within the
138 cytosolic extracts of *Drosophila* embryos with different affinities (Tovey et al., 2018). We found
139 that bacterially purified MBP-tagged N-terminal fragments of Cnn-T (MBP-Cnn-T-N) could
140 immunoprecipitate cytosolic γ-tubulin with a much higher affinity than the equivalent fragments
141 of Cnn-C (MBP-Cnn-C-N). Both isoforms share a short sequence just proximal to the CM1
142 domain (residues 78-97 in Cnn-C), but differ in their extreme N-terminal region, which is 77
143 residues long in Cnn-C but only 19 residues long in Cnn-T (dark blue and red, respectively, in
144 Figure 1A). While it is possible that that the difference in binding between the MBP-Cnn-C-N
145 and MBP-Cnn-T-N fragments could have been an artefact induced by bacterial purification,
146 we had hypothesised that the larger extreme N-terminal region of Cnn-C may fold back and
147 auto-inhibit the CM1 domain, restricting its ability to bind γ-TuRCs. To address this directly,
148 and to confirm the *in vitro* binding results, we developed an *in vivo* γ-TuRC recruitment assay
149 based on mRNA injection into *Drosophila* eggs. Using this assay, we could quickly and easily
150 manipulate the sequence of Cnn (without having to generate transgenic lines) and,
151 importantly, the folding of Cnn proteins would occur in a natural environment. The assay is
152 based on a previous experiment where we had injected mRNA encoding a GFP-tagged
153 phospho-mimetic form of Cnn into unfertilised *Drosophila* eggs to produce centrosome-like
154 scaffolds spontaneously throughout the cytosol. The phospho-mimetic mutations are placed
155 within the central PReM domain of Cnn-C (Cnn-C-PReM^{m}) and drive the oligomerisation of
156 GFP-Cnn-C molecules into the GFP-labelled scaffold structures (Conduit et al., 2014a) (Figure
157 1B; Figure S1). We realised that we could use these scaffolds to assess the ability of Cnn-C,
158 and any modified forms of Cnn-C (Figure 1B), to bind and recruit γ-TuRCs by examining the
159 recruitment of fluorescently-tagged γ-TuRC proteins to the scaffolds.

160

161 We first compared scaffolds formed from GFP-Cnn-C-PReM^{m} to scaffolds where the extreme
162 N-terminal region of Cnn-C-PReM^{m} was either exchanged with the extreme N-terminal region
163 of Cnn-T (GFP-Cnn-T-PReM^{m}) or was removed (GFP-Cnn-C$^{\Delta 1\text{-}77}$-PReM^{m}). For simplicity we
164 refer to these as Cnn-C, Cnn-T, and Cnn-C$^{\Delta 1\text{-}77}$ scaffolds, respectively, regardless of the
165 fluorescent tag used. In order to assess recruitment of γ-tubulin complexes to the scaffolds,
166 we endogenously tagged the maternal form of γ-tubulin with mCherry (γ-tubulin-37C-
167 mCherry) and injected unfertilised eggs laid by these mothers (we refer to γ-tubulin complexes
168 rather than γ-TuRCs, as it is possible that Cnn can bind and recruit γ-TuSCs as well as γ-
169 TuRCs). Initial visual observations suggested that γ-tubulin-37C-mCherry associated more

170 readily with Cnn-T and Cnn-C$^{\Delta 1\text{-}77}$ scaffolds than with Cnn-C scaffolds (Figure 1C-E). We
171 measured the GFP (Cnn) and mCherry (γ-tubulin-37C) fluorescence signals at multiple
172 scaffolds of different sizes and from different eggs and generated linear lines of best-fit (Figure
173 1F; see Methods for details). The slopes of these lines (S) are an estimation of the relative
174 binding affinity between the different Cnn constructs and γ-tubulin complexes. S values for the
175 various Cnn scaffolds differed significantly overall ($p<0.001$, $F_{2,354}=1645$) and also in pairwise
176 comparisons: the S value for Cnn-T scaffolds (0.55) was ~26-fold higher than the S value for
177 Cnn-C scaffolds (0.02) ($p<0.001$, $t_{350}=-57$) (Figure 1F), indicating that the N-terminal region of
178 Cnn-T binds γ-tubulin complexes with ~26-fold higher affinity than the N-terminal region of
179 Cnn-C, and confirming the results from our previous *in vitro* binding experiments (Tovey et al.,
180 2018). Importantly, the S value for Cnn-C$^{\Delta 1\text{-}77}$ scaffolds (0.17) was ~8-fold higher than the S
181 value for Cnn-C scaffolds ($p<0.001$, $t_{357}=36$) (Figure 1F), showing that removing the extreme
182 N-terminal region of Cnn-C increases binding affinity to γ-tubulin complexes by ~8 fold. This
183 therefore confirms that the extreme N-terminal region of Cnn-C is inhibitory for binding to γ-
184 tubulin complexes. Consistent with this, we also found that MBP-tagged N-terminal fragments
185 of Cnn-C$^{\Delta 1\text{-}77}$ (MBP-Cnn-C-N$^{\Delta 1\text{-}77}$) could immunoprecipitate γ-tubulin from embryo extracts
186 more efficiently than N-terminal fragments of Cnn-C (Figure 1G). Comparing the band
187 intensities (normalised to the γ-tubulin band in the MBP-Cnn-T-N IP lane, see Methods) of γ-
188 tubulin across three experiments showed that in this assay the truncated MBP-Cnn-C$^{\Delta 1\text{-}77}$-N
189 form bound nearly as well as MBP-Cnn-T-N (average normalised value of 0.90, Figure 1H).
190 Thus, while it is known that the CM1 domain is required for binding γ-tubulin complexes, we
191 find that the extreme N-terminal region of Cnn-C inhibits binding to γ-tubulin complexes; we
192 therefore name this region the "CM1 auto-inhibition" (CAI) domain.
193
194 Intriguingly, the *in vivo* assay also showed that the S value for Cnn-C$^{\Delta 1\text{-}77}$ scaffolds was ~3.3-
195 fold lower than that of Cnn-T scaffolds ($p<0.001$, $t_{357}=-21$) (Figure 1F), suggesting that the
196 extreme N-terminal region of Cnn-T (red in Figure 1A) promotes binding to γ-tubulin
197 complexes.
198
199 To test whether Cnn scaffolds recruit other γ-TuRC components, we assessed the ability of
200 mKATE-tagged Cnn-T scaffolds to recruit the γ-TuRC-specific components Grip75, Grip128,
201 and Grip163 (homologues of GCP4, 5 and 6, respectively) that we had endogenously tagged
202 with GFP (Figure 2). We again quantified the fluorescence signals at multiple scaffolds across
203 embryos and generated S values. We found that all S values for Cnn-T scaffolds were
204 significantly higher than the respective S values for Cnn-C scaffolds: fold change of 7.4 for

205 Grip75-sfGFP ($p<0.001$, $t_{365}=-28$) (Figure 2C), 6.7 for Grip128-sfGFP ($p<0.001$, $t_{349}=-37$)
206 (Figure 2F), and 2.2 for Grip163-sfGFP eggs ($p<0.001$, $t_{551}=-9$) (Figure 2I). The lower fold
207 changes as compared to γ-tubulin37C-mCherry could be a consequence of the lower signal-
208 to-noise ratios for Grip75-sfGFP, Grip128-sfGFP and Grip163-sfGFP due to their lower
209 stoichiometry within γ-TuRCs. Alternatively, the lower fold changes could be caused by a
210 proportion of γ-tubulin complexes bound by Cnn-T that do not contain Grip75, Grip128, or
211 Grip163, which would be the case if Cnn could bind and recruit both γ-TuSCs and γ-TuRCs.
212 Nevertheless, a combination of western blotting and mass spectrometry showed that
213 bacterially purified MBP-Cnn-T-N fragments could co-immunoprecipitate the γ-TuRC
214 components γ-tubulin, Grip71, Grip75, Grip84, Grip91, Grip128, Grip163 (Figure S2). We
215 therefore conclude that the Cnn-T N-terminus can bind γ-tubulin complexes containing γ-
216 TuRC-specific proteins.
217
218 **Cnn-T scaffolds organise microtubules more robustly than Cnn-C scaffolds**
219 If Cnn-T scaffolds can recruit functional γ-tubulin complexes, the scaffolds should be able to
220 nucleate and organise microtubules. We had previously shown that Cnn-C scaffolds could
221 organise microtubule asters, but only when these scaffolds were large (Conduit et al., 2014a).
222 To test whether microtubules are organised more robustly by Cnn-T scaffolds (which recruit
223 more γ-tubulin complexes than Cnn-C scaffolds) we formed scaffolds within eggs expressing
224 the microtubule binding protein Jupiter-mCherry (Figure 3A,B). We used a blind analysis to
225 quantify the propensity of these Cnn scaffolds to organise microtubules by categorising eggs
226 into those where the scaffolds organised “strong”, “medium”, “weak”, or no microtubule asters.
227 We also included a “tubulin overlay” category, where the Jupiter-mCherry signal did not extend
228 beyond the GFP scaffold signal. For simplicity, we refer to eggs containing Cnn-C and Cnn-T
229 scaffolds as Cnn-C and Cnn-T eggs, respectively. Consistent with the increased recruitment
230 of γ-tubulin complexes to Cnn-T scaffolds, we found that a higher proportion of Cnn-T eggs
231 (43.8%) than Cnn-C eggs (11.5%) contained scaffolds that organised strong or medium
232 microtubule asters (Figure 3C). Moreover, while 69.2% of Cnn-C eggs contained scaffolds
233 that did not organise any visible microtubule asters, none of the Cnn-T eggs fell into this
234 category (Figure 3C). Based on these differences, we conclude that the γ-tubulin complexes
235 recruited to Cnn scaffolds are able to nucleate microtubules, at least to some extent. The
236 ability of some Cnn-C scaffolds to organise microtubules is not unexpected, as these scaffolds
237 can still recruit low levels of γ-tubulin complexes (Figure 1C,F).
238

239 Filming the scaffolds through time revealed that scaffolds could merge and could also be quite
240 mobile, especially those that had microtubules emanating from just one side (Video 1). In
241 these instances, the microtubules appeared to push the scaffolds through the cytosol. Most
242 intriguingly, we could observe events where spindle-like structures formed between adjacent
243 Cnn-T scaffolds (Figure 3D). This was unexpected, but suggested that the microtubules
244 organised by the scaffolds are dynamic and can be regulated by motor proteins. We managed
245 to film the formation of these transient spindle-like structures (Video 2; Video 3), and in one
246 example multiple spindle-like structures formed simultaneously in close proximity and were
247 organised by a nearby group of coalescing scaffolds into a flower-like arrangement; the
248 spindles then quickly disappeared (Video 3). On some occasions, we could observe giant
249 Cnn-T scaffolds that organised large bundles of microtubules (Video 4). One of these giant
250 scaffolds rotated, dragging its associated microtubule bundles, indicating that the microtubules
251 were robustly anchored to the scaffolds, presumably via linkage by γ-tubulin complexes. In
252 summary, we conclude that Cnn-T scaffolds can recruit γ-tubulin complexes that are capable
253 of nucleating and anchoring microtubules.
254
255 **Phosphorylation of a conserved helix within the CAI domain, including a conserved**
256 **Polo kinase site, helps relieve auto-inhibition**
257 The data above shows that the extreme N-terminal CAI domain of Cnn-C inhibits binding to
258 γ-tubulin complexes. Given the similar length of the CAI and CM1 domains, we speculated
259 that the CAI domain may fold back over and inhibit the CM1 domain (Figure 4A). Given that
260 Cnn-C recruits γ-TuRCs to centrosomes (Zhang and Megraw, 2007; Conduit et al., 2014b)
261 and that Cnn-C is phosphorylated specifically at centrosomes and not within the cytosol
262 (Conduit et al., 2014a), we reasoned that CAI domain inhibition could be relieved by
263 phosphorylation, with negatively charged phosphate groups driving the separation of the CAI
264 and CM1 domains (Figure 4A). We therefore used sequence alignments and secondary
265 structure predictions of amino acids 1 to ~255 of Cnn-C from various *Drosophila* species to
266 search bioinformatically for potential phosphorylation sites (Figure S3). We identified three
267 putative phosphorylation "patches" based on a high concentration of often conserved serine
268 and threonine residues (Figure 4A; Figure S3). Patch 1 (P1) and Patch 2 (P2) lie within the
269 CAI domain and so are absent from Cnn-T; Patch 3 (P3) lies within the CM1 domain and so
270 is conserved between all Cnn isoforms. P1 also represented the only predicted structured
271 region within the CAI domain, corresponding to an α-helix (Figure S3).
272

273 We purified MBP-tagged N-terminal fragments of Cnn-C containing phosphomimetic
274 mutations in all serine and threonine residues within either P1 (MBP-Cnn-C-N^{P1}), P2 (MBP-
275 Cnn-C-N^{P2}), P3 (MBP-Cnn-C-N^{P3}), or in all three patches (MBP-Cnn-C-N^{P1-3}). We then
276 assessed how much γ-tubulin associated with these fragments compared with the original
277 MBP-Cnn-C-N (low binding) and MBP-Cnn-T-N (high binding) fragments when performing
278 anti-MBP immunoprecipitation. We found that MBP-Cnn-C-N^{P1} bound more γ-tubulin than
279 MBP-Cnn-C-N, but less than MBP-Cnn-T-N (Figure 4B). MBP-Cnn-C-N^{P2} also bound more γ-
280 tubulin than MBP-Cnn-C-N, although not as much as MBP-Cnn-C-N^{P1} (Figure 4B). In contrast
281 to P1 and P2, introducing mimetic mutations into P3 appeared to impede γ-TuRC binding.
282 Firstly, MBP-Cnn-C-N^{P3} bound less γ-tubulin compared to MBP-Cnn-C-N, and secondly MBP-
283 Cnn-C-N^{P1-3} bound less γ-tubulin compared to MBP-Cnn-C-N^{P1} (Figure 4B), suggesting that
284 the phosphomimetic insertions in P3 counteracted the positive effect of the phosphomimetic
285 insertions in P1 and P2. Quantifying γ-tubulin band intensities across 5 experiments showed
286 that while MBP-Cnn-C-N immunoprecipitated ~18% of γ-tubulin compared to MBP-Cnn-T-N,
287 MBP-Cnn-C-N^{P1} immunoprecipitated ~44% of γ-tubulin (Figure 4D). Thus, the data suggest
288 that phosphorylation of one or more sites within P1, and to a lesser extent P2, helps relieve
289 CAI domain-mediated auto-inhibition of Cnn-C's CM1 domain to allow the CM1 domain to bind
290 to γ-tubulin complexes.
291
292 Given that mimicking sites within P1 gave the strongest effect, we wanted to narrow down
293 which site or sites within P1 were important for relieving autoinhibition. There are six serine
294 and threonine residues within P1 (S^{21}, S^{22}, T^{27}, T^{31}, T^{33}, S^{34}) (Figure 4A; Figure S3). T^{27} is a
295 putative Polo site based on the surrounding residues that match the L/Φ-E/D/N/Q-X-S/T-Φ
296 consensus motif of Plk1 (the human homologue of Polo) (Santamaria et al., 2011). Moreover,
297 a previous study that mutated T^{27} to alanine within Cnn-C constructs reported microtubule
298 defects at centrosomes in *Drosophila* embryos (Eisman et al., 2015). We therefore generated
299 three different phospho-mimetic fragments, where either the proximal three residues (S^{21}, S^{22},
300 T^{27}) were mimicked (MBP-Cnn-C-N^{P1a}), the distal three residues (T^{31}, T^{33}, S^{34}) were mimicked
301 (MBP-Cnn-C-N^{P1b}), or only the predicted Polo site was mimicked (MBP-Cnn-C-N^{T27}). We
302 found that MBP-Cnn-C-N^{P1a} and MBP-Cnn-C-N^{T27} bound more γ-tubulin than MBP-Cnn-C-N,
303 but that this was not true of MBP-Cnn-C-N^{P1b} (Figure 4C). Quantification of γ-tubulin band
304 intensities from 5 experimental repeats indicated that MBP-Cnn-C-N^{T27} immunoprecipitated
305 ~34% of γ-tubulin compared to MBP-Cnn-T-N, which is more than for MBP-Cnn-C-N (~18%)
306 although less than when all sites within P1 are mimicked (~44%). This data suggests that
307 phosphorylation of multiple residues within P1, including the predicted Polo site at T^{27}, helps

308 to relieve CAI domain inhibition to allow binding to γ-tubulin complexes. This is consistent with
309 the microtubule defects previously observed at centrosomes in $T^{27}A$ mutant *Drosophila*
310 embryos (Eisman et al., 2015).
311
312 **Ubiquitous expression of Cnn-C containing the high binding-affinity Cnn-T N-terminal**
313 **region has a dominant negative effect and leads to fertility defects**
314 We next wanted to test whether Cnn-C auto-inhibition is important for cell and developmental
315 fidelity in *Drosophila*, as previous experiments in human and fission yeast cells have shown
316 that expression of CM1 domain fragments leads to ectopic cytosolic microtubule nucleation
317 (Choi et al., 2010; Lynch et al., 2014; Hanafusa et al., 2015; Cota et al., 2017). We generated
318 a transgenic fly line by random insertion of a ubiquitously-driven untagged Cnn-C construct in
319 which its N-terminal region had been replaced with the N-terminal region of Cnn-T (pUbq-Cnn-
320 C^T) (Figure 5A). We decided to use the N-terminal region of Cnn-T, rather than simply
321 removing the CAI domain or introducing phospho-mimetic mutations, as our *in vivo* and *in vitro*
322 assays had shown that this would allow the strongest and most consistent binding. As a control
323 we generated a line ubiquitously expressing untagged wild-type Cnn-C (pUbq-Cnn-C), whose
324 binding to cytosolic γ-tubulin complexes should be restricted by the CAI domain.
325
326 Consistent with the prediction that pUbq-Cnn-C^T would bind and activate cytosolic γ-tubulin
327 complexes, we found it difficult to generate a viable pUbq-Cnn-C^T line. We quickly discovered
328 that the pUbq-Cnn-C^T stock that we had generated was difficult to maintain and combine with
329 other alleles, presumably due to toxic effects caused by pUbq-Cnn-C^T expression. For
330 example, we were unable to generate a stock where pUbq-Cnn-C^T was expressed in a *cnn*
331 mutant background. Thus, all of the following experiments were performed with the pUbq
332 constructs expressed in the presence of endogenous Cnn.
333
334 We first tested the fertility rates of males and females bred at 25˚C, comparing them to the
335 pUbq-Cnn-C control stock. We quantified the hatching rate of embryos that were generated
336 when pUbq-Cnn-C or pUbq-Cnn-C^T males or females were crossed to w^{1118} "wild-type" flies.
337 Young (0-1 week old) pUbq-Cnn-C^T females produced embryos of which only 55% hatched,
338 compared to an average hatching rate of ~85% for embryos from young pUbq-Cnn-C females
339 (Figure 5B; $p<0.001$). Hatching rates for older (1-2 week old) females of both genotypes were
340 similar to the younger females (52.2% for pUbq-Cnn-C^T, 74.8% for pUbq-Cnn-C) and were
341 also significantly different from each other (Figure 5B; $p<0.001$). An even larger reduction in
342 hatching rate between pUbq-Cnn-C and pUbq-Cnn-C^T flies was observed when crossing

343 males. When young (0-1 week old) pUbq-Cnn-C^T males were crossed to wild-type females
344 only 40.3% of embryos hatched, compared to 84.7% when crossing pUbq-Cnn-C males
345 (Figure 5B; $p<0.001$). When older (1-2 week old) pUbq-Cnn-C^T males were crossed to wild-
346 type females only 9.9% of embryos hatched, compared to 90.5% for pUbq-Cnn-C males
347 (Figure 5B; $p<0.001$). Thus, the ability of both males and females to generate progeny is
348 reduced when ubiquitously expressing Cnn-C^T compared to Cnn-C, and males are more
349 strongly affected.
350
351 Given this difference between females and males, we tested whether the expression of the
352 two different pUbq constructs varies within female and male germlines. We used two different
353 Cnn antibodies to probe western blots for Cnn protein: one raised against the N-terminal half
354 of Cnn-C (aa1-660), the other against the C-terminal half (aa661-1147). The N-terminal
355 antibody recognises fewer unspecific bands on western blots, but its ability to bind Cnn-C^T
356 could be affected by the differences in the extreme N-terminal region of Cnn-T. Western
357 blotting extracts from wild-type, pUbq-Cnn-C, and pUbq-Cnn-C^T embryos or testes with either
358 the N-terminal or C-terminal Cnn-C antibody showed that each extract contained a Cnn-C
359 band at ~150kDa (Figure 5C). This band represents the endogenous form of Cnn-C in both
360 the wild-type and pUbq-Cnn-C^T extracts (black arrowheads, Figure 5C), but is a combination
361 of endogenous Cnn-C and pUbq-driven Cnn-C in the pUbq-Cnn-C extract (blue arrowhead,
362 Figure 5C), explaining why this band is much stronger in the pUbq-Cnn-C extract lanes. The
363 lower band in the pUbq-Cnn-C^T extract lanes is of an appropriate size for the slightly smaller
364 Cnn-C^T protein (red arrowheads, Figure 5C). The C-terminal antibody generated a weaker,
365 non-specific band of similar size to the Cnn-C^T band, which could be observed in the wild-type
366 and pUbq-Cnn-C lanes (asterisks). The unspecific nature of this band was highlighted by its
367 absence on membranes probed with the N-terminal Cnn antibody. Nevertheless, to confirm
368 that the lower bands in the pUbq-Cnn-C^T lanes do indeed represent Cnn-C^T, we generated an
369 isoform-specific antibody raised against a short peptide within the isoform-specific extreme N-
370 terminal exon of Cnn-T (anti-Cnn-T^N). This antibody recognised a single band of the expected
371 size only in the pUbq-Cnn-C^T extract lanes (Figure 5C), thus confirming the identity of the Cnn-
372 C^T band.
373
374 Importantly, there was a clear difference in the relative levels of pUbq-Cnn-C^T between
375 embryo and testes extracts. In the embryo extracts, the pUbq-Cnn-C^T band was much weaker
376 than the endogenous Cnn-C band, which is unusual for pUbq-driven Cnn constructs (P.
377 Conduit unpublished observations); presumably the intensity of the pUbq-Cnn-C^T band

378 observed when using the C-terminal antibody would have been even lower were it not for the
379 overlapping unspecific band recognised by this antibody. Indeed, the relative band intensity
380 of pUbq-Cnn-C^T is much lower when using the N-terminal antibody, although this could also
381 reflect a difference in the ability of this antibody to recognise the modified N-terminal region of
382 pUbq-Cnn-C^T. In contrast to embryo extracts, the pUbq-Cnn-C^T band was of a similar intensity
383 to, if not higher than, the endogenous Cnn-C band in the testes extracts. We therefore
384 conclude that, relative to endogenous Cnn-C, pUbq-Cnn-C^T is weakly expressed within the
385 maternal germline but is expressed to levels similar to endogenous Cnn within the testes.
386 While other factors could be involved, such as cell-specific effects of CM1 domain binding on
387 γ-tubulin complexes, differences in expression levels of pUbq-Cnn-C^T between cells could
388 explain the difference in the ability of male and female flies to generate progeny. Consistent
389 with this, it was easier to maintain the pUbq-Cnn-C^T stock at lower temperatures (where
390 expression is likely reduced).
391
392 **pUbq-Cnn-C^T binds to cytosolic γ-tubulin complexes with a higher affinity than pUbq-**
393 **Cnn-C**
394 We performed IP experiments to confirm that pUbq-Cnn-C^T binds γ-TuRCs more efficiently
395 than pUbq-Cnn-C, which would presumably account for the toxic effects. We tried using beads
396 coated with the anti-Cnn-T^N antibody but found that it did not pull down any protein (data not
397 shown), presumably as this antibody was raised against a peptide antigen and recognises
398 only denatured pUbq-Cnn-C^T on western blots. We therefore used beads coupled to Cnn-C
399 C-terminal antibodies, which should recognise both pUbq-Cnn-C and pUbq-Cnn-C^T equally
400 well. In order to compare the amount of γ-tubulin bound by each type of Cnn molecule, we
401 adjusted gel loading to reflect the differences in the expression levels of pUbq-Cnn-C and
402 pUbq-Cnn-C^T within embryos. We found that more γ-tubulin was immunoprecipitated with
403 pUbq-Cnn-C^T than with pUbq-Cnn-C, as expected (Figure 5D, right panels).
404
405 **Mis-regulation of binding to γ-tubulin complexes results in ectopic microtubule**
406 **nucleation and defects during cell division**
407 The failure to generate normal numbers of progeny suggested that ectopic binding of Cnn to
408 γ-tubulin complexes leads to cellular defects during germline or embryo development. We
409 therefore carried out immunostainings to examine directly any potential defects. We first fixed
410 and stained oocytes for markers of polarity, where specific microtubule arrangements are
411 required to establish and maintain polarity (Bastock and Johnston, 2008). In wild-type oocytes,
412 the nucleus is positioned in the dorsal corner from stage 8 to 10 and Staufen protein localises

413 in the centre of the oocyte at stage 8 and then at the posterior in stage 9 and 10. This was
414 true of all pUbq-Cnn-C (n=35, stage 8; n=35, stage 9; n=30, stage 10) and all pUbq-Cnn-C^T
415 (n=40, stage 8; n=50, stage 9; n=40, stage 10) oocytes (Figure S4A,B). Gurken protein is
416 normally positioned close to the nucleus in the dorsal corner of the oocyte and its mis-
417 positioning or its absence results in abnormal dorsal appendages that protrude from the
418 surface of the egg. Once again, we found that Gurken protein was localised normally in all
419 pUbq-Cnn-C (n=30) and all pUbq-Cnn-C^T (n=35) stage 9 oocytes (Figure S4C), and the dorsal
420 appendages were normal on all pUbq-Cnn-C (n=724) and all pUbq-Cnn-C^T (n=488) eggs. We
421 therefore conclude that there are no severe microtubule organisation defects in pUbq-Cnn-C^T
422 oocytes and that polarity is normally established.
423
424 We next stained early embryos laid by either wild-type, pUbq-Cnn-C, or pUbq-Cnn-C^T females
425 for DNA, microtubules, and γ-tubulin. Prior to cellularisation, embryos go through 13 rounds
426 of rapid and near-synchronous mitotic divisions within a syncytium. Centrosomes are
427 constantly in a “mature” state and centrosomal microtubules help coordinate rearrangements
428 of the actin network that in turn ensures the correct spacing of nuclei and microtubule-based
429 spindles. In theory, ectopic nucleation of cytosolic microtubules could interfere with this
430 process, as well as spindle formation. We therefore performed a blind analysis of pUbq-Cnn-
431 C or pUbq-Cnn-C^T embryos categorising each embryo into those with severe, moderate, mild,
432 or no defects, depending on both the broadness of defects across the embryo and how severe
433 individual defects appeared. We found that a higher percentage of both pUbq-Cnn-C and
434 pUbq-Cnn-C^T embryos fell into the severe and moderate categories compared to wild-type
435 embryos, but that a higher proportion of pUbq-Cnn-C^T embryos than pUbq-Cnn-C embryos
436 fell into the severe category (Figure 5E). Broadly, the categorisation reflects the observed
437 hatching rates in Figure 5B. Cytosolic non-centrosomal microtubules appeared to be present
438 within ~10.8% of pUbq-Cnn-C^T embryos, but this was very similar in pUbq-Cnn-C embryos
439 (~9.6%). Nevertheless, this suggests that ectopic binding of γ-tubulin complexes by Cnn
440 (either due to the presence of unregulated Cnn-C^T or due to overexpression of Cnn-C) can
441 lead to ectopic microtubule nucleation in at least a fraction of embryos.
442
443 To directly test whether Cnn binding to γ-tubulin complexes could initiate ectopic cytosolic
444 microtubule nucleation within embryos, we injected mRNA encoding the N-terminal region of
445 Cnn-T tagged with GFP (GFP-Cnn-T-N) into unfertilised eggs expressing the microtubule
446 marker Jupiter-mCherry. We injected into eggs rather than fertilised embryos to avoid
447 complications caused by centrosomes and mitotic figures that would have been present in

448 developing embryos. Strikingly, live imaging revealed the presence of highly dynamic
449 microtubules throughout the cytosol within eggs injected with GFP-Cnn-T-N mRNA that were
450 not observed within eggs injected with water (Video 5). Thus, it appears that binding of Cnn
451 to γ-tubulin complexes can stimulate ectopic microtubule nucleation within these
452 eggs/embryos, similar to how binding of the CM1 domain can stimulate ectopic cytosolic
453 microtubule nucleation within human cells (Choi et al., 2010; Cota et al., 2017; Hanafusa et
454 al., 2015) and fission yeast (Lynch et al., 2014).
455
456 We next examined testes from pUbq-Cnn-C^T males, which were less able to generate progeny
457 than pUbq-Cnn-C^T females. Production of sperm involves a series of mitotic and meiotic cell
458 divisions followed by sperm elongation within the testes (Fabian and Brill, 2012). Mutations in
459 *cnn* or γ-TuRC genes lead to defects during the two meiotic divisions (Vogt et al., 2006; Li et
460 al., 1998). These defects can be quickly revealed by using phase contrast microscopy to
461 examine round spermatids, which are the cells produced immediately after the meiotic
462 divisions. Round spermatids exist as interconnected cysts of 64 cells with each cell normally
463 containing a single round phase-light nucleus and a single round phase-dark mitochondrial
464 derivative (nebenkern) of similar size (Figure 5G). Problems in spindle formation can lead to
465 mis-segregation of chromosomes during meiosis (karyokinesis defects), and this can result in
466 nuclei of variable size between different cells within the same cyst and, when major problems
467 occur, to cells containing multiple or no nuclei. Cytokinesis defects can also result in cells
468 containing the wrong number of nuclei. Nebenkerns assemble from mitochondria that are also
469 equally distributed by the spindle during cell division, and so defects in spindle formation and
470 cytokinesis also lead to variations in nebenkern size and number. We therefore quantified and
471 compared the variability in nuclear size within cysts (as a marker of karyokinesis defects) and
472 the nucleus:nebenkern ratio (as a marker of major karyokinesis defects and/or cytokinesis
473 defects). We found that the variability in nuclear size was larger within pUbq-Cnn-C^T testes
474 compared to pUbq-Cnn-C testes (Figure 5H). Moreover, while the nucleus:nebenkern ratio
475 was always close to 1 in pUbq-Cnn-C testes, it varied between 0.5 and 1.75 in pUbq-Cnn-C^T
476 testes (Figure 5H). Thus, major karyokinesis and cytokinesis defects exist within pUbq-Cnn-
477 C^T testes.
478
479 To examine this more directly, we fixed and stained the testes for DNA, microtubules, and the
480 centriole marker Asterless (Asl). Consistent with the phase contrast imaging of round
481 spermatids, we observed examples of major karyokinesis and cytokinesis defects during
482 meiosis in pUbq-Cnn-C^T testes (Figure 5I; Figure S5). For example, the middle panel of Figure

483 5I shows a pUbq-Cnn-C^T cell in telophase of meiosis I where cleavage furrow ingression had
484 failed or was delayed and where both sets of daughter chromosomes had ended up on the
485 same side of the cell, rather than being partitioned between the two future daughter cells. The
486 right panel shows an example of a cell in metaphase of meiosis II that contained two spindles
487 (instead of one) with one centriole at each pole. Presumably this cell had failed cytokinesis
488 after meiosis I. This cell also contained ectopic clusters of microtubules within the cytosol away
489 from the centrosomes, suggesting that microtubules had been nucleation randomly within the
490 cytosol. These ectopic clusters of microtubules were observed in other pUbq-Cnn-C^T
491 spermatocytes at different cell cycle stages (Figure S5). We conclude that expressing pUbq-
492 Cnn-C^T, which can bind γ-tubulin complexes away from centrosomes, leads to major defects
493 during male meiosis due to ectopic nucleation of microtubules within the cytosol.
494

495 ## Discussion

496 We propose a molecular model for the spatiotemporal regulation of γ-tubulin complex binding
497 by Cnn-C during cell division in *Drosophila*. In this model, Cnn-C is prevented from binding γ-
498 tubulin complexes within the cytosol by its extreme N-terminal region that we name the CM1-
499 autoinhibition (CAI) domain. We propose that the CAI domain folds back to sterically inhibit
500 the CM1 domain, and that this inhibition is relieved only once Cnn-C is recruited to
501 centrosomes and phosphorylated at sites within the CAI domain, including the predicted Polo
502 site T^{27}. This mechanism explains why Cnn-C does not normally bind γ-Tubulin complexes
503 within the cytosol, which can lead to ectopic microtubule nucleation and major defects during
504 cell division.
505
506 In contrast to Cnn-C, we show that the testes-specific isoform of Cnn, Cnn-T, binds cytosolic
507 γ-tubulin complexes with high affinity. We now show that this difference is largely due to the
508 presence of the CAI domain at the extreme N-terminus of Cnn-C, which is absent from Cnn-
509 T due to differential exon splicing. Removal of the CAI domain from Cnn-C increases binding
510 to cytosolic γ-TuRCs. Moreover, phospho-mimicking sites in a conserved α-helix within the
511 CAI domain, including the putative Polo kinase site at T^{27}, also allows increased binding to γ-
512 tubulin complexes, presumably by relieving the auto-inhibition to some degree. We previously
513 showed that Cnn-C is phosphorylated only at centrosomes during cell division with Polo
514 phosphorylating sites within the central PReM domain to drive Cnn oligomerisation and
515 centrosome scaffold assembly (Conduit et al., 2014a; Feng et al., 2017). Our new data
516 presented here suggests that Polo also phosphorylates the CAI domain, presumably
517 specifically at centrosomes, to spatially regulate binding to γ-tubulin complexes. Coupling of
518 centrosome scaffolding and γ-tubulin complex binding via Polo phosphorylation provides an
519 elegant way for the cell to control proper spindle formation during cell division.
520
521 While phospho mimicking residues within P1 quantifiably increased binding to γ-tubulin
522 complexes, binding was less efficient than with N-terminal fragments of Cnn-T. There are
523 several possibilities for this. Cnn-C may never bind as strongly to γ-tubulin complexes as Cnn-
524 T, perhaps because other proteins can support recruitment of γ-tubulin complexes to the
525 centrosome. It is possible that a very particular combination of phosphorylation events within
526 P1, or P1 and P2, must occur, and that we have not yet tried those combinations. Perhaps
527 the phospho-mimetic mutations do not fully mimic natural phosphorylation events, which is
528 anecdotally common. Alternatively, other regulatory events, possibly dependent on other
529 proteins, may need to occur. These events could help the unfolding of the CAI domain or they

530 could mediate the binding of the CAI domain to γ-tubulin complexes after unfolding occurs.
531 We note that phospho-mimicking either all sites within P1, or T27 alone, did not result in
532 increased recruitment of γ-tubulin to Cnn scaffolds in the majority of eggs in our *in vivo*
533 recruitment assay (data not shown). It is therefore possible that in the presence of full length
534 Cnn-C that is oligomerising into scaffolds, other regulatory events become even more
535 important. Nevertheless, our data still support a model in which phosphorylation of residues
536 within P1, including T^{27}, help to relieve CAI-domain mediated auto-inhibition.
537
538 While T^{27} has not been identified in phospho-mapping mass spectrometry (Dinkel et al., 2010;
539 Zhai et al., 2008; Conduit et al., 2014a; Bodenmiller et al., 2008), it has previously been
540 identified bioinformatically as a potential Polo kinase site (Eisman et al., 2015). In their study,
541 the authors mutated T^{27} and an adjacent putative Polo docking site (S^{22}) to prevent putative
542 phosphorylation and found defects in microtubule organisation at centrosomes in *Drosophila*
543 syncytial embryos (Eisman et al., 2015), consistent with our model. While we have
544 demonstrated that phospho-mimicking T^{27} is sufficient to increase binding to γ-tubulin
545 complexes, we have so far been unable to phosphorylate T^{27} *in vitro* using recombinant human
546 Plk1 kinase. We suspect that this could be because other phosphorylation events must first
547 occur, such as phosphorylation of S^{22} within the putative Polo docking site, or that human Plk1
548 cannot replace fly Polo in these *in vitro* assays.
549
550 It will be interesting to see whether the CAI domain is functionally conserved through evolution.
551 While sequence similarity outside the CM1 domain is very low, CM1-domain proteins from
552 different species tend to contain extended N-terminal regions (Lin et al., 2014b), and the
553 lengths of these regions can vary between isoforms, similar to the length differences between
554 Cnn-C and Cnn-T. A study analysing budding yeast Spc110 showed that phosphorylation of
555 Cdk1 and Mps1 phosphorylation sites in the region proximal to the CM1 domain promoted
556 binding to γ-TuSCs and subsequent oligomerisation of γ-TuSCs *in vitro* (Lin et al., 2014b),
557 although a later study questioned the effect of these phosphorylation sites (Lyon et al., 2016).
558 The binding between human CDK5RAP2 and γ-TuRCs also appears to be regulated by
559 phosphorylation. It was shown that depletion of LLRK1 kinase, which functions downstream
560 of Plk1, reduced the ability of N-terminal fragments of CDK5RAP2 (aa51-200) to co-
561 immunoprecipitate γ-tubulin from HEK293 cells, and also reduced the ability of these
562 fragments to promote ectopic microtubule nucleation within the cytosol (which is dependent
563 on γ-TuRC binding) (Hanafusa et al., 2015). In contrast to *Drosophila* Cnn-C, however, the
564 phosphorylation site identified as being important for γ-TuRC binding is located downstream

565 of the CM1 domain (S140). Nevertheless, it remains possible that this downstream region, in
566 place of, or in combination with, the region upstream of the CM1 domain, could fold back over
567 the CM1 domain and function in an equivalent manner to the CAI domain within *Drosophila*
568 Cnn. Clearly, CDK5RAP2 must somehow be prevented from binding cytosolic γ-TuRCs, and
569 this will have to be addressed in future.
570
571 While we have focussed on how the binding between Cnn-C and γ-tubulin complexes is
572 regulated during cell division, our data also highlights differences in how binding is regulated
573 between cell types and MTOCs. We have shown both here and previously (Tovey et al., 2018)
574 that the testes specific Cnn-T isoform, which lacks the CAI domain, binds efficiently to γ-tubulin
575 complexes in the apparent absence of any upstream regulatory events. Cnn-T is expressed
576 primarily within developing sperm cells and isoform-specific C-terminal exons mediate its
577 recruitment to mitochondria, where it binds and recruits γ-tubulin complexes (Chen et al.,
578 2017). The mitochondrial surface is very different from mature centrosomes, which
579 concentrate a selection of kinases, including Polo. It therefore seems appropriate that Cnn-T
580 isoforms splice out the exons that comprise the CAI domain to ensure that phosphorylation is
581 not required for γ-tubulin complex binding. Presumably, binding and potential activation of γ-
582 tubulin complexes within the shrinking cytosol of developing sperm cells is not detrimental to
583 sperm development (and may even be important for amplifying cytoplasmic microtubules),
584 unlike in dividing cells where our data shows that spindle formation and cytokinesis are clearly
585 perturbed.
586
587 Intriguingly, our data suggest that Cnn-T binds γ-tubulin complexes with a higher affinity than
588 a truncated version of Cnn-C lacking the inhibitory CAI domain. This shows that the Cnn-T
589 specific extreme N-terminal exon (red in Figure 1A) promotes binding. It also suggests that
590 binding within sperm cells might be stronger than binding at centrosomes within dividing cells.
591 Our preferred interpretation, however, is that the CAI domain, once unfolded from the CM1
592 domain, may promote γ-tubulin complex binding once its inhibitory role has been relieved,
593 possibly by direct binding or by binding to other proteins that support γ-tubulin complex
594 binding. This is consistent with observations in budding yeast, where removal of SPC110's N-
595 terminal region up to the CM1 domain reduces its binding affinity to γ-TuSCs (Lyon et al.,
596 2016).
597
598 There is currently some debate as to how the binding of CM1-domain proteins influences the
599 activity of γ-tubulin complexes. There is good evidence from different labs that expression of

600 human N-terminal CDK5RAP2 fragments containing either a part of or the whole CM1 domain
601 results in random microtubule nucleation throughout the cytosol (Choi et al., 2010; Muroyama
602 et al., 2016; Hanafusa et al., 2015). This effect is dependent on the ability of these fragments
603 to bind γ-tubulin complexes within the cytosol (Choi et al., 2010) and on LRKK1 kinase, which
604 facilitates binding (Hanafusa et al., 2015). Thus, binding of cytosolic γ-tubulin complexes by
605 CDK5RAP2 appears to promote the ability of the γ-tubulin complexes to nucleate
606 microtubules. This is also true in fission yeast, where a truncated form of Mto1 lacking MTOC
607 localisation domains but containing the CM1 domain formed puncta within the cytosol that
608 nucleated microtubules (Lynch et al., 2014). In *Drosophila*, ectopic expression of Cnn-T in
609 cultured fly cells converts mitochondria to MTOCs capable of nucleating microtubules (Chen
610 et al., 2017). Based on these studies, the CM1 domain has been regarded as an activator of
611 γ-tubulin complexes. Two recent papers, however, reported only a small increase in
612 microtubule nucleation from purified human or *Xenopus* γ-TuRCs after addition of CM1-
613 domain fragments (Liu et al., 2019; Thawani et al., 2020). Moreover, recent cryo-EM data
614 shows no evidence for structural changes when purified human or *Xenopus* γ-TuRCs are
615 bound by CM1-domain fragments (Wieczorek et al., 2019; Liu et al., 2019). Nevertheless, one
616 of these studies did show that adding CM1-domain fragments to purified γ-TuRCs within
617 *Xenopus* egg extracts supplemented with activated Ran resulted in a dramatic increase in
618 microtubule aster formation (Liu et al., 2019), suggesting that specific conditions may be
619 required for the activating ability of the CM1 domain. Taken together, the data from different
620 reports suggest that binding of the CM1 domain can increase the propensity of γ-tubulin
621 complexes to nucleate microtubules, but how this occurs and whether it is context specific
622 remains unclear.
623
624 The idea that CM1-domain binding may promote γ-tubulin complex activity in a context-
625 specific manner is consistent with our *in vivo* data showing that ectopic binding of cytosolic γ-
626 TuRCs by Cnn leads to major defects during male meiosis but apparently to less severe
627 defects in embryos and no obvious polarity defects in oocytes. These differences, however,
628 could be due to the observed differences in expression levels of pUbq-Cnn-C^T between cell
629 types. They may also be due to variation in the ability of different cell types to cope with
630 increased cytosolic microtubule nucleation. For example, signals that control cleavage plane
631 positioning and furrow ingression during cytokinesis are mediated by direct contacts between
632 both astral microtubules and central spindle microtubules and the cell cortex (D'Avino et al.,
633 2015). It is easy to imagine how ectopically nucleated microtubules, that could interact at
634 random with the cell cortex, could interfere with cytokinesis of spermatocytes during

635 *Drosophila* male meiosis. Oocytes that already contain a large number of microtubules
636 throughout the cytosol and early embryos where nuclei divide within a syncytium may be less
637 severely affected.
638
639 In summary, we have revealed molecular details that help explain how microtubule nucleation
640 is spatially controlled to ensure fidelity of cell division and development. Our work encourages
641 future research to investigate how binding of γ-tubulin complexes by CM1-domain proteins is
642 regulated in other species and how this binding leads to microtubule nucleation.
643

644 # Materials and Methods

645

646 **DNA cloning**

647 5-alpha competent *E. coli* cells (high efficiency, NEB) were used for bacterial transformations.
648 DNA fragments were purified using QIAquick Gel Extraction kits (Qiagen); plasmid purification
649 was performed using QIAprep Spin Miniprep kits (Qiagen). Phusion high-fidelity PCR master
650 mix with HF buffer (ThermoFisher Scientific) was used for PCRs.

651

652 **Transgenic *Drosophila* lines**

653 All endogenously-tagged lines were made using CRISPR combined with homologous
654 recombination, by combining the presence of a homology-repair vector containing the desired
655 insert with the appropriate guide RNAs and Cas9. The γ-tubulin37C-mCherry and Grip128-
656 sfGFP alleles were generated by inDroso. For γ-tubulin37C-mCherry, eggs from nos-Cas9
657 expressing females were co-injected with a plasmid encoding the expression of dual guides
658 targeting each side of the 3'UTR, TACACATATCAAGATACATG and
659 CCCAGATCGATTATCCCCAG, and a plasmid containing a SSSS-mCherry-3'UTR-LoxP-
660 3xP3-dsRED-Lox P cassette flanked by homology arms (the multi-serine insert acts as a
661 flexible linker). After screening for dsRED, the selection marker was excised by Cre
662 recombination. For Grip128-sfGFP, eggs from nos-Cas9 expressing females were co-injected
663 with a plasmid encoding the expression of a single guide containing the target sequence
664 ATGGGGCACACTGGAGTTGA and with a pBluescript plasmid containing sfGFP and linker
665 sequence (4X GlyGlySer) flanked on either side by 1.5kb of DNA homologous to the genomic
666 locus surrounding the 3' end of the appropriate coding region. The homology vector was made
667 within the lab (and sent to InDroso) by HiFi assembly (NEB) of PCR fragments generated from
668 genomic DNA prepared from nos-Cas9 flies (using MicroLYSIS, Microzone) and a vector
669 containing the sfGFP tag (DGRC, 1314). Screening for the insert was performed with the
670 following primers: AGGAAGATGCGAACACACGT and GTACAGCTCATCCATGCCCA.

671

672 The Grip75-sfGFP and Grip163-sfGFP lines were made within the lab following a similar
673 approach to that used previously (Tovey et al., 2018; Mukherjee et al., 2020). Flies expressing
674 a single guide RNA containing the target sequence CAAAAACATCGTATTCATG or
675 ACCACTATTACAAGGTATCT for Grip75-sfGFP or Grip163-sfGFP, respectively, were
676 crossed to nos-Cas9 expressing females and the resulting embryos were injected with
677 homology vectors by the Department of Genetics Fly Facility, Cambridge, UK. The homology
678 vectors comprised a pBluescript plasmid containing sfGFP and linker sequence (4X

679 GlyGlySer) flanked on either side by 1.5kb of DNA homologous to the genomic locus
680 surrounding the 3' end of the appropriate coding region. The homology vectors were made as
681 for Grip128-sfGFP. F1 and F2 males were screened by PCR using the following primers: for
682 Grip75-sfGFP: GAGAAGTTTGCGCATATGACCC and AGCAGCACCATGTGATCGCGC; for
683 Grip163-sfGFP: AGTCGCAGTCCTTTATTGTGG and
684 AGCAGCACCATGTGATCGCGC.
685
686 pUbq-Cnn-C and pUbq-Cnn-C^T were made from a pDONR-Cnn-C vector (gift from Jordan
687 Raff). To generate a Cnn-T-specific N-terminal region of Cnn, an appropriate DNA fragment
688 (made by Genewiz, based on the FlyBase sequence of Cnn-T) was synthesised and amplified
689 by PCR and used to replace the N-terminal region of Cnn in a pDONR-Cnn-C vector cut with
690 XmaI. The pDONR-Cnn-C and newly made pDONR-Cnn-T vectors were then inserted into a
691 pUbq transformation vector (gift from Jordan Raff) by Gateway cloning (ThermoFisher
692 Scientific). All DNA vectors were injected into embryos by the Department of Genetics Fly
693 Facility, Cambridge, UK.
694
695 **Recombinant protein expression and purification**
696 Fragments of Cnn-C-N and Cnn-T-N were amplified from the pDONR-Cnn-C and pDONR-
697 Cnn-T vectors described above by PCR and inserted into a pDEST-HisMBP (Addgene,
698 #11085) vector by Gateway cloning (Thermo Fisher Scientific). Proteins were expressed in *E.*
699 *coli* (BL21-DE3) and purified using affinity chromatography. MBP-tagged fragments were
700 purified by gravity flow through amylose resin (New England Biolabs) and step elution in
701 maltose. The concentration of each fraction was determined on a Nanodrop and peak fractions
702 were diluted 1:1 with glycerol and stored at -20°C.
703
704 Phosphomimetic fragments were created by modifying the pDONR-Cnn-C-N entry clone. The
705 backbone was linearised by PCR or by digestion, omitting the phospho-patch to be replaced,
706 and phosphomimetic patches in which all S/T residues were swapped for D/E residues,
707 respectively, were synthesised by PCR using two overlapping primers and were inserted by
708 NEB HiFi Assembly. The entry clones were checked by restriction enzyme digest and
709 sequencing before being inserted into the pDEST-HisMBP destination vector via a Gateway
710 reaction.
711
712 Truncated fragments of Cnn-C were made by modification of the pDONR-Cnn-C-N entry
713 clone. The N-terminal region was removed by a Quikchange reaction (Agilent), and the

714 resulting shortened fragment was inserted into the pDEST-HisMBP destination vector via a
715 Gateway reaction.
716
717 pRNA vectors were made by modification of the pDONR-Cnn-C-PReM^{P} vector containing
718 phospho-mimetic mutations in the PReM domain (Conduit et al., 2014a). N-terminal variants
719 were introduced by restriction digests (SspI-HF and AatII) of pDONR-Cnn-C, pDONR-Cnn-T,
720 and Cnn-C-PReM^{P} entry clones. Fragments were combined as necessary by NEB HiFi
721 assembly to create new pDONR vectors, which were inserted into a pRNA-GFP or pRNA-
722 mKate destination vector (Conduit et al., 2014a) via a Gateway reaction. The Cnn-T-N
723 fragment was inserted directly into pRNA-GFP destination vectors via Gateway cloning.
724
725 **Primers**

	Forward primer	**Reverse primer**
Cnn-C-N fragment	GGGGACAAGTTTGTACAAAAAAGCAGGCTTAATGGACCAGTCTAAACAGGTTTTGC	GGGGACCACTTTGTACAAGAAAGCTGGGTTCTATAGGCGCTCGGCCAAC
Cnn-T-N fragment	GGGGACAAGTTTGTACAAAAAAGCAGGCTTAATGAATAGTAATCGAACGTCGTCTTCG	GGGGACCACTTTGTACAAGAAAGCTGGGTTCTATAGGCGCTCGGCCAAC
Cnn-C-N^{P1} insert	GCGGGACTATTGCGGCGACGGCAATGGTACCTGTGCAGACGACTTGAAGGAAATCGAGTTAATTGAGGAGGTGG	GCAGGACCCTTCTGTCGATTTCGGCGGCGCCATTCTCCTCCAGGAAGTCCTCCACCTCCTCAATTAACTCGATTTCC
Cnn-C-N^{P2} insert	CCTGCGCAAACTAGCCGAGGCACTGGACAAAGACATAGACGACGAGGACCCGGGAGCCCTGCAAGATGTCG	CGCCTGGAGGTCGTGGAACGTCAAAGTCGGCATAGTCGTTCTCCATCTCGACATCTTGCAGGGCTCCCGGGTCC
Cnn-C-N^{P3} insert	GGGTCAGCCGGGTGCCCGGGCAGACGACGACGAGGAAGACTTAGACAAACAGCTCATCGATGCCAAGATCGAAATCGC	CCTTGAGCAGCTCCATCTTTACATCGACCTCTTTTCTCAACTCCGCGATTTCGATCTTGGCATCGATGAGC
Cnn-C-N^{P1a} insert	GCGGGACTATTGCGGCGACGGCAATGGTACCTGTGCAGACGACTTGAAGGAAATCGAGTTAATTGAGACCGTGA	GGACCCTTCTGTCGATTTCGGCGGCGCCATTCTCCTCCAGGAAACTGGTCACGGTCTCAATTAACTCGATTTCCTTC

Cnn-C-N^{P1b} insert	GCGGGACTATTGCGGCGACGGCAATGGTACCTGTGCATCGTCCTTGAAGGAAATCACCTTAATTG	GGACCCTTCTGTCGATTTCGGCGGCGCCATTCTCCTCCAGGAAGTCCTCCACCTCCTCAATTAAGGTGATTTCCTTC
Cnn-C-N^{T27} insert	GCGGGACTATTGCGGCGACGGCAATGGTACCTGTGCATCGTCCTTGAAGGAAATCGAGTTAATTGAGACCGTGA	GGACCCTTCTGTCGATTTCGGCGGCGCCATTCTCCTCCAGGAAACTGGTCACGGTCTCAATTAACTCGATTTCCTTC
Cnn-C-N$^{\Delta 1\text{-}77}$	GCCAACTTTGTACAAAAAAGCAGGCTTAATGGCCAGTTTTGACGTTCC	GGAACGTCAAAACTGGCCATTAAGCCTGCTTTTTTGTACAAAGTTGGC

Immunoprecipitation

1g/ml of embryos were homogenised with a hand-pestle in homogenisation buffer containing 50 mM HEPES, pH7.6, 1mM $MgCl_2$, 1 mM EGTA, 50 mM KCl supplemented with PMSF 1:100, Protease Inhibitor Cocktail (1:100, Sigma Aldrich) and DTT (1M, 1:1000). Extracts were clarified by centrifugation twice for 15 minutes at 16,000 rcf at 4°C.

For the MBP-Cnn fragment IPs, 30 µl magnetic ProteinA dynabeads (Life Technologies) coupled to anti-MBP antibodies (gift from Jordan Raff) were incubated with an excess of purified MBP-Cnn fragments and rotated for 1 hour at 4°C. Unbound fragments were washed off in PBST, and the saturated beads were resuspended in 100 µl embryo extract and rotated at 4°C overnight. Beads were washed 5 times for 1 min each in PBST, boiled in 2x sample buffer, and separated from the sample using a magnet. Samples were analysed by western blotting as described below.

For the Grip-GFP IPs, 20 µl high-capacity ProteinA beads (Abcam) coupled to anti-MBP antibodies (gift from Jordan Raff) were incubated with an excess of purified MBP-Cnn fragments and rotated at 4°C for 1 hour. Unbound fragments were washed off in PBST and the saturated beads were resuspended in 65 µl embryo extract and rotated at 4°C overnight. Beads were washed 5 times for 1 min each in PBST, boiled in 2x sample buffer, and separated from the sample by centrifugation. Samples were analysed by western blotting as described below.

750 For the IPs from pUbq-Cnn-C and pUbq-Cnn-C^T embryo extract, 50 µl magnetic ProteinA
751 dynabeads (Life Technologies) coupled to anti-Cnn (C-terminal) antibodies (gift from Jordan
752 Raff) were rotated at 4°C for 1 hour. Unbound fragments were washed off in PBST and the
753 saturated beads were resuspended in 100 µl embryo extract and rotated at 4°C overnight.
754 Beads were washed 5 times for 1 min each in PBST, boiled in 2x sample buffer, and separated
755 from the sample using a magnet. Samples were analysed by western blotting as described
756 below.
757
758 **Electrophoresis and western blotting**
759 Samples were run on 4-20% TGX Precast Gels (BioRad) (except Figure 5C and D, in which
760 samples were run on 7.5% TGX Precast gels (BioRad)), alongside 5µl Precision Plus
761 WesternC Standard markers (BioRad). For western blotting, semi-dry blotting was carried out
762 using TransBlot Turbo 0.2µm nitrocellulose membrane transfer packs (BioRad), and a
763 TransBlot Turbo transfer system running at 1.3A, up to 25V, for 7 minutes (BioRad mixed
764 molecular weight pre-set programme). Membranes were stained with Ponceau, washed, first
765 with distilled water then with milk solution (PSBT + 4% milk powder), and then blocked in milk
766 solution for 1 hour at room temperature. Sections of blots were incubated with primary
767 antibodies as indicated in figures (antibodies found in table). Blots were incubated with
768 horseradish peroxidase (HRP)-conjugated anti-mouse, anti-rabbit, or anti-sheep secondary
769 antibodies (1:2000 in PSBT + 4% milk powder, ImmunoReagents) as appropriate for 45 mins
770 at room temperature, washed in PSBT for 3 times for 15 mins each, and then incubated with
771 ECL substrate (BioRad ECL Clarity or ThermoFisher SuperSignal West Femto Max) for 5
772 minutes. Membranes were imaged using a Kodak Image Station 4000R.
773
774 **Mass spectrometry**
775 Samples were run 1 cm into the lanes of 4-20% TGX Precast Gels (BioRad). Gels were rinsed
776 in dH_2O and lanes were excised using a clean razor blade and cut into $1mm^2$ pieces on a fresh
777 glass slide, destained if necessary, reduced (DTT) and alkylated (iodoacetamide) and
778 subjected to enzymatic digestion with sequencing grade trypsin (Promega, Madison, WI, USA)
779 overnight at 37°C. After digestion, the supernatant was pipetted into a sample vial and loaded
780 onto an autosampler for automated LC-MS/MS analysis.
781
782 *LC-MS/MS.* All LC-MS/MS experiments were performed using a Dionex Ultimate 3000 RSLC
783 nanoUPLC (Thermo Fisher Scientific Inc, Waltham, MA, USA) system and a Q Exactive
784 Orbitrap mass spectrometer (Thermo Fisher Scientific Inc, Waltham, MA, USA). Separation

785 of peptides was performed by reverse-phase chromatography at a flow rate of 300 nL/min
786 using a Thermo Scientific reverse-phase nano Easy-spray column (Thermo Scientific PepMap
787 C18, 2 µm particle size, 100A pore size, 75 µm i.d. x 50cm length). Peptides were initially
788 loaded onto a pre-column (Thermo Scientific PepMap 100 C18, 5 µm particle size, 100Å pore
789 size, 300 µm i.d. x 5mm length) from the Ultimate 3000 autosampler with 0.1% formic acid for
790 3 minutes at a flow rate of 10 µL/min. After this period, the column valve was switched to allow
791 elution of peptides from the pre-column onto the analytical column. Solvent A was water +
792 0.1% formic acid and solvent B was 80% acetonitrile, 20% water + 0.1% formic acid. The
793 linear gradient employed was 2-40% B in 30 minutes. Further wash and equilibration steps
794 gave a total run time of 60 minutes.
795
796 The LC eluant was sprayed into the mass spectrometer by means of an Easy-Spray source
797 (Thermo Fisher Scientific Inc.). All *m/z* values of eluting ions were measured in an Orbitrap
798 mass analyzer, set at a resolution of 70000 and was scanned between *m/z* 380-1500. Data
799 dependent scans (Top 20) were employed to automatically isolate and generate fragment ions
800 by higher energy collisional dissociation (HCD, NCE:25%) in the HCD collision cell and
801 measurement of the resulting fragment ions was performed in the Orbitrap analyser, set at a
802 resolution of 17500. Singly charged ions and ions with unassigned charge states were
803 excluded from being selected for MS/MS and a dynamic exclusion window of 20 seconds was
804 employed.
805
806 *Database searching.* Post-run, all MS/MS data were converted to mgf files and the files were
807 then submitted to the Mascot search algorithm (Matrix Science, London UK, version 2.6.0)
808 and searched against the Uniprot Drosophila_melanogaster_20180813 database (23297
809 sequences; 16110808 residues) and common contaminant sequences containing non-
810 specific proteins such as keratins and trypsin (123 sequences; 40594 residues). Variable
811 modifications of oxidation (M), deamidation (NQ) and phosphorylation (S,T and Y) were
812 applied as well a fixed modification of carbamidomethyl (C). The peptide and fragment mass
813 tolerances were set to 20ppm and 0.1 Da, respectively. A significance threshold value of
814 $p<0.05$ and a peptide cut-off score of 20 were also applied.
815
816 **Antibodies**
817 Primary antibodies used in the study are indicated in the table below. For western blotting,
818 primary and secondary antibodies were diluted in PBST + 4% milk; primary antibodies were
819 diluted at concentrations indicated in the table; secondary antibodies were diluted at 1:2000.

820 For immunostaining, primary and secondary antibodies were diluted in PBS + 0.1% Triton
821 (PBT) + 5% BSA; primary antibodies were diluted at concentrations indicated in the table;
822 secondary antibodies (AlexaFluor 488, 561, or 633 conjugated secondary antibodies
823 (ThermoFisher)) were diluted at 1:1000 for testes and 1:1500 for embryos. DNA was stained
824 with Hoechst (Life Technologies, 33342) or DAPI.
825

Antibody	WB Concentration	IF Concentration	Source
α-Tubulin mouse monoclonal	-	1:1000	Sigma Aldrich, DM1a
Asl (N-terminal) guinea pig polyclonal	1:1000	1:1000	Gift from Jordan Raff
Cnn (N-terminal) rabbit monoclonal	1:1000	1:1000	Gift from Jordan Raff
Cnn (C-terminal) sheep polyclonal	1:1000	-	Gift from Jordan Raff
Cnn-T^N Rabbit polyclonal	1:500	-	This study
γ-Tubulin mouse monoclonal	1:500	1:500	Sigma Aldrich, GTU-88
γ-Tubulin rabbit polyclonal	-	1:500	Sigma Aldrich, T5192
GFP mouse monoclonal	1:250 or 1:500	1:250 or 1:500	Roche, 11814460001
Grip71 rabbit polyclonal	1:100	1:100	CRB (crb2005268)
MBP rabbit polyclonal	1:3000	-	Gift from Jordan Raff
Phospho-histone H3 rabbit polyclonal	-	1:500	Abcam, AB5176
Staufen Mouse monoclonal	-	1:100	Santa Cruz dN-16
Gurken Mouse monoclonal	-	1:200	DSHB 1D12
Lamin Dm0	-	1:30	DSHB 84.12

826
827 **Immunostaining**
828 Testes were dissected in PBS, fixed in 4% paraformaldehyde for 30 minutes, washed 3x 5
829 minutes in PBS and incubated in 45% and then 60% acetic acid before being squashed onto
830 slides and flash-frozen in liquid nitrogen. Coverslips were removed and samples were post-
831 fixed in methanol at -20°C, washed 3x 15 minutes in PBS + 0.1% Triton (PBST), then

832 incubated overnight in a humid chamber at 4°C with primary antibodies diluted in PBST + 5%
833 BSA + 0.02% azide. Slides were washed 3x 5 minutes in PBST and then incubated for 2 hours
834 at room temperature with Alexa-Fluor secondary antibodies (ThermoFisher) (all 1:1000 in
835 PBST + 5% BSA + 0.02% azide). Slides were washed 3x 15 minutes in PBST, 10 minutes in
836 PBST with Hoechst, and then 5 minutes in PBST. 10 µl of mounting medium (85% glycerol in
837 H_20 + 2.5% N-propyl-galate) was placed on top of the tissue and a coverslip was gently
838 lowered and sealed with nail varnish.
839
840 Embryos were collected within 2-3 hours of laying and were dechorionated in 60% bleach for
841 2 minutes. Vitelline membranes were punctured with a combination heptane and methanol +
842 3% EGTA (0.5M) before three washes in neat methanol. Embryos were fixed in methanol at
843 4°C for at least 24 hours before rehydrating. Embryos were rehydrated by washing 3x 20 mins
844 in PBST, then blocked in PBST + 5% BSA for 1 hour, followed by overnight incubation in
845 primary antibodies in PBST + 5% BSA at 4°C. Embryos were washed 3x 20 mins in PBST at
846 room temperature, then incubated for 2 hours at room temperature with Alexa-Fluor secondary
847 antibodies (ThermoFisher) (all 1:1500 in PBST + 5% BSA). Finally, embryos were washed 3x
848 20 mins in PBST at room temperature before being mounted in Vectashield containing DAPI
849 (VectorLabs).
850
851 Oocytes were dissected from 2-day-old females. For Staufen and Gurken detection, 10 to 15
852 ovaries were fixed with PBS buffer containing 4% paraformaldehyde and 0.1% Triton X-100,
853 washed three times for 5 mins in PBST (PBS+0.1% Triton X-100) and blocked in PBST
854 containing 1% BSA. Incubation with the primary antibodies (anti-Staufen, Santa Cruz; anti-
855 Gurken 1D12, DSHB) was performed overnight at room temperature or 4°c for Staufen and
856 Gurken labelling, respectively, in PBT (PBS containing 0.1% BSA and 0.1% Tween 20). The
857 ovaries were then briefly washed three times and three times for 30 min each in BBT and
858 incubated for 2 hours at room temperature in Alexa-conjugated secondary antibodies. The
859 ovaries were then washed 3x for 15 min each time in PBST, dissected, and mounted in
860 Citifluor (Electron Microscopy Science).
861
862 **Phase contrast imaging of round spermatids**
863 For analysis of round spermatids under phase contrast, testes were dissected in PBS,
864 transferred to a 50µl droplet of PBS on a slide, cut open midway along the testes and, under
865 observation, gently squashed under a coverslip using blotting paper.
866

867 **RNA preparation and injection**

868 pRNA vectors containing the appropriate cDNA were generated using Gateway cloning of
869 PCR amplified cDNA and either a pRNA-GFP or a pRNA-mKATE backbone. pRNA vectors
870 were linearised with AscI, precipitated using EDTA, sodium acetate, and ethanol, then
871 resuspended in RNase-free water. mRNA was generated from these pRNA vectors *in vitro*
872 using a T3 mMESSAGE mMACHINE kit (ThermoFisher) and was then purified using an
873 RNeasy MinElute Cleanup kit (Qiagen). Freshly-laid early embryos, or unfertilised eggs, were
874 collected from apple juice plates within 15-30 minutes of laying and were dechorionated on
875 double-sided sticky tape. Embryos/eggs were lined up on heptane glue to keep them in place
876 during injections and imaging. Embryos were dried at 25°C for 5 mins and covered with
877 immersion oil (Voltalef). RNA was injected into embryos/eggs using needles made from
878 borosilicate glass capillary tubes, at a final concentration of ~2 µg/µl. Embryos/unfertilised
879 eggs were left for 1-2 hours before imaging to allow for translation of the mRNA.

880

881 **Microscopy**

882 Confocal imaging of Cnn scaffolds organising microtubules and of fixed embryo and testes
883 samples was carried out on an Olympus FV3000 scanning inverted confocal system run by
884 FV-OSR software using a x60 1.4NA silicone immersion lens (UPLSAPO60xSilicone) or x30
885 0.95NA silicone immersion lens (UPLSAPO30xSilicone). Confocal imaging of oocytes was
886 carried out on a Zeiss LSM700 confocal microscope. Epifluorescence microscopy of Cnn
887 scaffolds recruiting γ-TuRC components and phase contrast microscopy of round spermatids
888 was performed on a Leica DM IL LED inverted microscope controlled by µManager software
889 and coupled to a RetigaR1 monochrome camera (QImaging) and a CoolLED pE-300 Ultra
890 light source using a 63X 1.3NA oil objective or a 40X 0.55NA air objective, respectively.

891

892 **Fertility tests**

893 Cages that were sealed with apple juice agar plates with a spot of dried yeast paste were set
894 up at 25°C containing ~50 newly-hatched test flies (e.g. pUbq-Cnn-C/ -C^T) and ~50 newly-
895 hatched wild-type males or virgin females. The apple juice agar plates were exchanged with
896 fresh plates 2-4 times a day, and the removed plates were kept at 25°C for at least 25 hours
897 before the proportion of hatched eggs was calculated.

898

899 **Image analysis**

900 All images were processed using Fiji (ImageJ). Maximum intensity Z-plane projections were
901 used to quantify the intensity of Cnn and γ-TuRC components at Cnn scaffolds, and intensities

902 of each channel at each scaffold were corrected for cytoplasmic background intensity.
903 Background intensity subtraction was also performed for quantification of western blot band
904 intensities. Within each experiment, the intensities of the γ-tubulin IP bands were normalised
905 to the intensity of the γ-tubulin band in the MBP-Cnn-T-N IP. Images of Cnn scaffolds
906 organising microtubules within eggs and of stained pUbq-Cnn-C or pUbq-Cnn-C^T embryos
907 were analysed blind to allow unbiased categorisation.
908
909 **Statistical analysis**
910 Most statistical analysis and all graph production were performed using GraphPad Prism 7 or
911 8. Analysis of Cnn scaffolds was carried out in the R programming language (https://www.r-
912 project.org/) using the emmeans package. The fluorescent signals at Cnn scaffolds were
913 collected from multiple embryos but included measurements from multiple scaffolds from
914 individual embryos. For linear regression analysis we therefore needed to use a mixed effects
915 model to take account of the 'repeated' measurements from individual embryos. The raw data
916 was not Normally distributed and was log transformed prior to performing the linear regression
917 analysis. An iterative process was used to explore the best model, which revealed that a
918 straight-line relationship best fitted the raw data and that regression lines should pass through
919 the origin (0;0). This could have been expected given the biological prediction that an increase
920 in Cnn intensity should result in a linear increase in the intensity of a γ-TuRC component. For
921 the final model, we transformed the data by taking the log of the γ-tubulin/Cnn ratio. The
922 graphs plotted for scaffold data are presented with raw data points with an overlay of the line
923 of best fit calculated by the linear mixed effects model. In the case where more than two lines
924 were being compared, Tukey's Test was used to compare the pairwise differences.
925
926 **Bioinformatics**
927 Protein alignments were produced using JalView. Secondary structure predictions were
928 performed using JPred 4.
929
930

931 ## Acknowledgements

932 This work was supported by a Wellcome Trust and Royal Society Sir Henry Dale fellowship
933 (105653/Z/14/Z) awarded to PTC, a Glover Fund research fellowship (Clare College/Dept. of
934 Biochemistry, University of Cambridge) awarded to CAT, and an Association pour la
935 Recherche sur le Cancer grant (PJA 20181208148) awarded to AG. We thank Jordan Raff for
936 sharing Cnn antibodies and plasmids, Berthold Hedwig and Steve Rogers for help with needle

pulling, and Matt Castle for guidance on statistical analysis of Cnn scaffolds. We thank other members of the Conduit lab for their invaluable input and critical reading of the manuscript. The work benefited from use of the Imaging Facility, Department of Zoology, supported by Matt Wayland and a Sir Isaac Newton Trust Research Grant (18.07ii(c)), and also from use of the Cambridge Centre for Proteomics Core Facility.

Author Contributions

PTC and CAT designed the study and wrote the manuscript. CAT carried out cloning for all experiments and performed the *in vitro* recruitment assays, fertility tests, embryo analysis, and round spermatid analysis. CT performed the majority of mRNA injection experiments and analysed the scaffold data. AE helped establish the mRNA assay. AG performed the oocyte analysis and analysed the data. FB and AG generated the γ-tubulin-mCherry fly line. MDR prepared bacterial cultures and assisted with protein purification.

Declaration of Interests

The authors declare no competing interests.

References

Akhmanova, A., and M.O. Steinmetz. 2015. Control of microtubule organization and dynamics: two ends in the limelight. *Nat Rev Mol Cell Bio*. 16:711 726. doi:10.1038/nrm4084.

Bastock, R., and D.S. Johnston. 2008. Drosophila oogenesis. *Curr Biol*. 18:R1082 7. doi:10.1016/j.cub.2008.09.011.

Bodenmiller, B., D. Campbell, B. Gerrits, H. Lam, M. Jovanovic, P. Picotti, R. Schlapbach, and R. Aebersold. 2008. PhosphoPep--a database of protein phosphorylation sites in model organisms. *Nat Biotechnol*. 26:1339 1340. doi:10.1038/nbt1208-1339.

Chen, J.V., R.A. Buchwalter, L.-R. Kao, and T.L. Megraw. 2017. A Splice Variant of Centrosomin Converts Mitochondria to Microtubule-Organizing Centers. *Curr Biol*. 27:1928 1940.e6. doi:10.1016/j.cub.2017.05.090.

967 Choi, Y.-K., P. Liu, S.K. Sze, C. Dai, and R.Z. Qi. 2010. CDK5RAP2 stimulates microtubule nucleation
968 by the γ-tubulin ring complex. *J Cell Biology*. 191:1089–1095. doi:10.1083/jcb.201007030.

969 Conduit, P.T., Z. Feng, J.H. Richens, J. Baumbach, A. Wainman, S.D. Bakshi, J. Dobbelaere, S.
970 Johnson, S.M. Lea, and J.W. Raff. 2014a. The centrosome-specific phosphorylation of Cnn by
971 Polo/Plk1 drives Cnn scaffold assembly and centrosome maturation. *Dev Cell*. 28:659 669.
972 doi:10.1016/j.devcel.2014.02.013.

973 Conduit, P.T., J.H. Richens, A. Wainman, J. Holder, C.C. Vicente, M.B. Pratt, C.I. Dix, Z.A. Novak,
974 I.M. Dobbie, L. Schermelleh, and J.W. Raff. 2014b. A molecular mechanism of mitotic centrosome
975 assembly in Drosophila. *Elife*. 3:2987. doi:10.7554/elife.03399.

976 Consolati, T., J. Locke, J. Roostalu, J. Asthana, W.M. Lim, J. Gannon, F. Martino, A. Costa, and T.
977 Surrey. 2019. Microtubule Nucleation by Single Human γTuRC in a Partly Open Asymmetric
978 Conformation. *Biorxiv*. 853218. doi:10.1101/853218.

979 Consolati, T., J. Locke, J. Roostalu, Z.A. Chen, J. Gannon, J. Asthana, W.M. Lim, F. Martino, M.A.
980 Cvetkovic, J. Rappsilber, A. Costa, and T. Surrey. 2020. Microtubule Nucleation Properties of
981 Single Human γTuRCs Explained by Their Cryo-EM Structure. *Dev Cell*.
982 doi:10.1016/j.devcel.2020.04.019.

983 Cota, R.R., N. Teixidó-Travesa, A. Ezquerra, S. Eibes, C. Lacasa, J. Roig, and J. Lüders. 2017. MZT1
984 regulates microtubule nucleation by linking γTuRC assembly to adapter-mediated targeting and
985 activation. *J Cell Sci*. 130:jcs.195321. doi:10.1242/jcs.195321.

986 D'Avino, P.P., M.G. Giansanti, and M. Petronczki. 2015. Cytokinesis in Animal Cells. *Csh Perspect*
987 *Biol*. 7:a015834. doi:10.1101/cshperspect.a015834.

988 Dinkel, H., C. Chica, A. Via, C.M. Gould, L.J. Jensen, T.J. Gibson, and F. Diella. 2010. Phospho.ELM:
989 a database of phosphorylation sites--update 2011. *Nucleic Acids Res*. 39:D261-7.
990 doi:10.1093/nar/gkq1104.

991 Eisman, R.C., M.A.S. Phelps, and T. Kaufman. 2015. An Amino-Terminal Polo Kinase Interaction
992 Motif Acts in the Regulation of Centrosome Formation and Reveals a Novel Function for
993 centrosomin (cnn) in Drosophila. *Genetics*. 201:685 706. doi:10.1534/genetics.115.181842.

994 Eisman, R.C., M.A.S. Phelps, and T.C. Kaufman. 2009. Centrosomin: a complex mix of long and short
995 isoforms is required for centrosome function during early development in Drosophila melanogaster.
996 *Genetics*. 182:979 997. doi:10.1534/genetics.109.103887.

997 Fabian, L., and J.A. Brill. 2012. Drosophila spermiogenesis. *Spermatogenesis*. 2:197–212.
998 doi:10.4161/spmg.21798.

999 Farache, D., L. Emorine, L. Haren, and A. Merdes. 2018. Assembly and regulation of γ-tubulin
1000 complexes. *Open Biol*. 8:170266. doi:10.1098/rsob.170266.

1001 Feng, Z., A. Caballe, A. Wainman, S. Johnson, A.F.M. Haensele, M.A. Cottee, P.T. Conduit, S.M. Lea,
1002 and J.W. Raff. 2017. Structural Basis for Mitotic Centrosome Assembly in Flies. *Cell*. 169:1078
1003 1089.e13. doi:10.1016/j.cell.2017.05.030.

1004 Flor-Parra, I., A.B. Iglesias-Romero, and F. Chang. 2018. The XMAP215 Ortholog Alp14 Promotes
1005 Microtubule Nucleation in Fission Yeast. *Curr Biol*. 28:1681 1691.e4.
1006 doi:10.1016/j.cub.2018.04.008.

1007 Goshima, G., M. Mayer, N. Zhang, N. Stuurman, and R.D. Vale. 2008. Augmin: a protein complex
1008 required for centrosome-independent microtubule generation within the spindle. *J Cell Biology*.
1009 181:421–429. doi:10.1083/jcb.200711053.

1010 Gunzelmann, J., D. Rüthnick, T. Lin, W. Zhang, A. Neuner, U. Jäkle, and E. Schiebel. 2018. The
1011 microtubule polymerase Stu2 promotes oligomerization of the γ-TuSC for cytoplasmic microtubule
1012 nucleation. *Elife*. 7:934. doi:10.7554/elife.39932.

1013 Hanafusa, H., S. Kedashiro, M. Tezuka, M. Funatsu, S. Usami, F. Toyoshima, and K. Matsumoto. 2015.
1014 PLK1-dependent activation of LRRK1 regulates spindle orientation by phosphorylating
1015 CDK5RAP2. *Nat Cell Biol*. 17:1024–1035. doi:10.1038/ncb3204.

1016 Hutchins, J.R.A., Y. Toyoda, B. Hegemann, I. Poser, J.-K. Hériché, M.M. Sykora, M. Augsburg, O.
1017 Hudecz, B.A. Buschhorn, J. Bulkescher, C. Conrad, D. Comartin, A. Schleiffer, M. Sarov, A.
1018 Pozniakovsky, M.M. Slabicki, S. Schloissnig, I. Steinmacher, M. Leuschner, A. Ssykor, S. Lawo,
1019 L. Pelletier, H. Stark, K. Nasmyth, J. Ellenberg, R. Durbin, F. Buchholz, K. Mechtler, A.A. Hyman,
1020 and J.-M. Peters. 2010. Systematic Analysis of Human Protein Complexes Identifies Chromosome
1021 Segregation Proteins. *Science*. 328:593–599. doi:10.1126/science.1181348.

1022 Kollman, J.M., C.H. Greenberg, S. Li, M. Moritz, A. Zelter, K.K. Fong, J.-J. Fernandez, A. Sali, J.
1023 Kilmartin, T.N. Davis, and D.A. Agard. 2015. Ring closure activates yeast γTuRC for species-
1024 specific microtubule nucleation. *Nat Struct Mol Biol*. 22:132 137. doi:10.1038/nsmb.2953.

1025 Kollman, J.M., A. Merdes, L. Mourey, and D.A. Agard. 2011. Microtubule nucleation by γ-tubulin
1026 complexes. *Nat Rev Mol Cell Bio*. 12:709 721. doi:10.1038/nrm3209.

1027 Lawo, S., M. Bashkurov, M. Mullin, M.G. Ferreria, R. Kittler, B. Habermann, A. Tagliaferro, I. Poser,
1028 J.R.A. Hutchins, B. Hegemann, D. Pinchev, F. Buchholz, J.-M. Peters, A.A. Hyman, A.-C. Gingras,
1029 and L. Pelletier. 2009. HAUS, the 8-subunit human Augmin complex, regulates centrosome and
1030 spindle integrity. *Curr Biol*. 19:816 826. doi:10.1016/j.cub.2009.04.033.

1031 Li, K., E.Y. Xu, J.K. Cecil, F.R. Turner, T.L. Megraw, and T.C. Kaufman. 1998. Drosophila
1032 centrosomin protein is required for male meiosis and assembly of the flagellar axoneme. *The Journal*
1033 *of cell biology*. 141:455 467.

1034 Lin, T., A. Neuner, and E. Schiebel. 2014a. Targeting of γ-tubulin complexes to microtubule organizing
1035 centers: conservation and divergence. *Trends Cell Biol*. 25:296 307. doi:10.1016/j.tcb.2014.12.002.

1036 Lin, T., A. Neuner, Y.T. Schlosser, E. Schiebel, A.N. Scharf, and L. Weber. 2014b. Cell-cycle
1037 dependent phosphorylation of yeast pericentrin regulates γ-TuSC-mediated microtubule nucleation.
1038 *Elife*. 3:e02208. doi:10.7554/elife.02208.

1039 Liu, P., Y.-K. Choi, and R.Z. Qi. 2014. NME7 is a functional component of the γ-tubulin ring complex.
1040 *Mol Biol Cell*. 25:2017–2025. doi:10.1091/mbc.e13-06-0339.

1041 Liu, P., E. Zupa, A. Neuner, A. Böhler, J. Loerke, D. Flemming, T. Ruppert, T. Rudack, C. Peter, C.
1042 Spahn, O.J. Gruss, S. Pfeffer, and E. Schiebel. 2019. Insights into the assembly and activation of the
1043 microtubule nucleator γ-TuRC. *Nature*. 1–8. doi:10.1038/s41586-019-1896-6.

1044 Lynch, E.M., L.M. Groocock, W.E. Borek, and K.E. Sawin. 2014. Activation of the γ-Tubulin Complex
1045 by the Mto1/2 Complex. *Curr Biol*. 24:896 903. doi:10.1016/j.cub.2014.03.006.

1046 Lyon, A.S., G. Morin, M. Moritz, K.C.B. Yabut, T. Vojnar, A. Zelter, E. Muller, T.N. Davis, and D.A.
1047 Agard. 2016. Higher-order oligomerization of Spc110p drives γ-tubulin ring complex assembly.
1048 *Mol Biol Cell*. 27:mbc.E16-02-0072 2258. doi:10.1091/mbc.e16-02-0072.

1049 Mukherjee, A., P.S. Brooks, F. Bernard, A. Guichet, and P.T. Conduit. 2020. Microtubules originate
1050 asymmetrically at the somatic Golgi and are guided via Kinesin2 to maintain polarity in neurons.
1051 *Elife*. 9:e58943. doi:10.7554/elife.58943.

1052 Muroyama, A., L. Seldin, and T. Lechler. 2016. Divergent regulation of functionally distinct γ-tubulin
1053 complexes during differentiation. *J Cell Biology*. 213:679–692. doi:10.1083/jcb.201601099.

1054 Nithianantham, S., B.D. Cook, M. Beans, F. Guo, F. Chang, and J. Al-Bassam. 2018. Structural basis
1055 of tubulin recruitment and assembly by microtubule polymerases with Tumor Overexpressed Gene
1056 (TOG) domain arrays. *Elife*. 7:e38922. doi:10.7554/elife.38922.

1057 Oegema, K., C. Wiese, O.C. Martin, R.A. Milligan, A. Iwamatsu, T.J. Mitchison, and Y. Zheng. 1999.
1058 Characterization of two related Drosophila gamma-tubulin complexes that differ in their ability to
1059 nucleate microtubules. *The Journal of cell biology*. 144:721 733.

1060 Petry, S., and R.D. Vale. 2015. Microtubule nucleation at the centrosome and beyond. *Nat Cell Biol*.
1061 17:1089 1093. doi:10.1038/ncb3220.

1062 Pinyol, R., J. Scrofani, and I. Vernos. 2013. The role of NEDD1 phosphorylation by Aurora A in
1063 chromosomal microtubule nucleation and spindle function. *Curr Biol*. 23:143 149.
1064 doi:10.1016/j.cub.2012.11.046.

1065 Sanchez, A.D., and J.L. Feldman. 2016. Microtubule-organizing centers: from the centrosome to non-
1066 centrosomal sites. *Curr Opin Cell Biol*. 44:93 101. doi:10.1016/j.ceb.2016.09.003.

1067 Santamaria, A., B. Wang, S. Elowe, R. Malik, F. Zhang, M. Bauer, A. Schmidt, H.H.W. Silljé, R.
1068 Körner, and E.A. Nigg. 2011. The Plk1-dependent Phosphoproteome of the Early Mitotic Spindle.
1069 *Mol Cell Proteomics*. 10:M110.004457. doi:10.1074/mcp.m110.004457.

1070 Sawin, K.E., P.C.C. Lourenço, and H.A. Snaith. 2004. Microtubule nucleation at non-spindle pole body
1071 microtubule-organizing centers requires fission yeast centrosomin-related protein mod20p. *Curr*
1072 *Biol*. 14:763 775. doi:10.1016/j.cub.2004.03.042.

1073 Scrofani, J., T. Sardon, S. Meunier, and I. Vernos. 2015. Microtubule nucleation in mitosis by a
1074 RanGTP-dependent protein complex. *Curr Biol*. 25:131 140. doi:10.1016/j.cub.2014.11.025.

1075 Tariq, A., L. Green, J.C.G. Jeynes, C. Soeller, and J.G. Wakefield. 2020. In vitro reconstitution of
1076 branching microtubule nucleation. *Elife*. 9:e49769. doi:10.7554/elife.49769.

1077 Teixidó-Travesa, N., J. Roig, and J. Lüders. 2012. The where, when and how of microtubule nucleation
1078 - one ring to rule them all. *J Cell Sci*. 125:4445 4456. doi:10.1242/jcs.106971.

1079 Thawani, A., R.S. Kadzik, and S. Petry. 2018. XMAP215 is a microtubule nucleation factor that
1080 functions synergistically with the γ-tubulin ring complex. *Nat Cell Biol*. 20:1 18.
1081 doi:10.1038/s41556-018-0091-6.

1082 Thawani, A., M.J. Rale, N. Coudray, G. Bhabha, H.A. Stone, J.W. Shaevitz, and S. Petry. 2020. The
1083 transition state and regulation of γ-TuRC-mediated microtubule nucleation revealed by single
1084 molecule microscopy. *Elife*. 9:e54253. doi:10.7554/elife.54253.

1085 Tillery, M., C. Blake-Hedges, Y. Zheng, R. Buchwalter, and T. Megraw. 2018. Centrosomal and Non-
1086 Centrosomal Microtubule-Organizing Centers (MTOCs) in Drosophila melanogaster. *Cells*. 7:121.
1087 doi:10.3390/cells7090121.

1088 Tovey, C.A., and P.T. Conduit. 2018. Microtubule nucleation by γ-tubulin complexes and beyond.
1089 *Essays Biochem*. 91:EBC20180028. doi:10.1042/ebc20180028.

1090 Tovey, C.A., C.E. Tubman, E. Hamrud, Z. Zhu, A.E. Dyas, A.N. Butterfield, A. Fyfe, E. Johnson, and
1091 P.T. Conduit. 2018. γ-TuRC Heterogeneity Revealed by Analysis of Mozart1. *Curr Biol*. 28:2314
1092 2323.e6. doi:10.1016/j.cub.2018.05.044.

1093 Uehara, R., R. Nozawa, A. Tomioka, S. Petry, R.D. Vale, C. Obuse, and G. Goshima. 2009. The augmin
1094 complex plays a critical role in spindle microtubule generation for mitotic progression and
1095 cytokinesis in human cells. *Proc National Acad Sci*. 106:6998 7003. doi:10.1073/pnas.0901587106.

1096 Vogt, N., I. Koch, H. Schwarz, F. Schnorrer, and C. Nüsslein-Volhard. 2006. The γTuRC components
1097 Grip75 and Grip128 have an essential microtubule-anchoring function in the Drosophila germline.
1098 *Development*. 133:3963–3972. doi:10.1242/dev.02570.

1099 Wieczorek, M., L. Urnavicius, S.-C. Ti, K.R. Molloy, B.T. Chait, and T.M. Kapoor. 2019. Asymmetric
1100 Molecular Architecture of the Human γ-Tubulin Ring Complex. *Cell*.
1101 doi:10.1016/j.cell.2019.12.007.

1102 Zhai, B., J. Villén, S.A. Beausoleil, J. Mintseris, and S.P. Gygi. 2008. Phosphoproteome analysis of
1103 Drosophila melanogaster embryos. *J Proteome Res*. 7:1675 1682. doi:10.1021/pr700696a.

1104 Zhang, J., and T.L. Megraw. 2007. Proper recruitment of gamma-tubulin and D-TACC/Msps to
1105 embryonic Drosophila centrosomes requires Centrosomin Motif 1. *Mol Biol Cell*. 18:4037 4049.
1106 doi:10.1091/mbc.e07-05-0474.

1107 Zhu, H., J.A. Coppinger, C.-Y. Jang, J.R. Yates, and G. Fang. 2008. FAM29A promotes microtubule
1108 amplification via recruitment of the NEDD1–γ-tubulin complex to the mitotic spindle. *J Cell*
1109 *Biology*. 183:835–848. doi:10.1083/jcb.200807046.

1110

1111 # Figure Legends

1112

1113 **Figure 1**

1114 **The extreme N-terminal region of Cnn-C inhibits binding to γ-tubulin complexes.** (**A**)
1115 Diagram of the centrosomal Cnn (Cnn-C) and testes-specific Cnn (Cnn-T) isoforms that exist
1116 *in vivo*. **(B)** Diagram of artificial Cnn proteins with differing N-terminal regions that were used
1117 to form Cnn scaffolds (induced by phospho-mimetic mutations in the PReM domain (beige))
1118 via mRNA injection into unfertilised eggs. **(C-E)** Fluorescence images of unfertilised eggs
1119 expressing γ-tubulin37C-mCherry that were injected with mRNA encoding the different types
1120 of artificial Cnn protein, as indicated. Insets show representative examples of individual
1121 scaffolds. **(F)** Graph showing fluorescence intensity measurements of γ-tubulin37C-mCherry
1122 and GFP-Cnn at Cnn scaffolds of different types (a.u., arbitrary units). Linear lines of best fit
1123 are shown. **(G,H)** Western blot (G) and quantification of γ-tubulin bands (H) showing
1124 immunoprecipitation of γ-tubulin from embryo extracts by bacterially-purified, MBP-tagged
1125 Cnn-C-N, Cnn-T-N and Cnn-$C^{\Delta 1\text{-}77}$-N fragments. The blot was probed with anti-MBP and anti-
1126 γ-tubulin antibodies, as indicated. Band intensities were normalised within each of 3
1127 experimental repeats to the γ-tubulin band in the respective MBP-Cnn-T-N IP.

1128

1129 **Figure 2**

1130 **Multiple γ-TuRC-specific proteins are recruited to Cnn-T scaffolds.** Fluorescence images
1131 **(A,B,D,E,G,H)** and graphs **(C,F,I)** showing recruitment of Grip75-sfGFP (A-C), Grip128-sfGFP
1132 (D-F), or Grip163-sfGFP (G-I) to either mKATE-Cnn-C or mKATE-Cnn-T scaffolds. Insets in
1133 (A,B,D,E,G,H) show representative examples of individual scaffolds. Fluorescence values in
1134 (C,F,I) are arbitrary units (a.u.). Linear lines of best fit are shown. In each case, the mKATE-
1135 Cnn-T scaffolds recruited more of the sfGFP-tagged Grip protein than the mKATE-Cnn-C
1136 scaffolds.

1137

1138 **Figure 3**

1139 **Cnn-T scaffolds organise microtubules more robustly than Cnn-C scaffolds. (A-C)**
1140 Fluorescence images (A,B) of Cnn-C scaffolds (A) or Cnn-T scaffolds (B) formed within eggs
1141 expression the microtubule marker Jupiter-mCherry. **(C)** Bar-graph showing quantification of
1142 a blind categorisation of eggs containing Cnn-C or Cnn-T scaffolds with regard to the ability
1143 of the scaffolds within the eggs to organise microtubule asters. The results show that Cnn-T
1144 scaffolds tend to organise microtubule asters more readily than Cnn-C scaffolds. **(D)**

1145 Fluorescence images showing that adjacent Cnn-T scaffolds can organise spindle-like
1146 structures.
1147
1148 **Figure 4**
1149 **Phosphorylation of the CAI domain relieves auto-inhibition to allow binding to γ-tubulin**
1150 **complexes. (A)** A hypothesis of how the CM1 domain (purple) might be sterically inhibited by
1151 folding back of the CAI domain (dark blue). Putative phospho-patches (containing high
1152 concentrations of Serine and Threonine residues) are indicated in yellow. The amino acid
1153 sequence of each putative phospho-patch is displayed with S and T residues highlighted in
1154 orange and the proportion of S and T residues within each patch indicated in brackets.
1155 Potential Polo kinase sites (green), Cdk1 sites (blue), and kinase landing sites (black) are
1156 indicated. **(B-D)** Western blots (B,C) and quantification of γ-tubulin bands (D) showing the
1157 immunoprecipitation of γ-tubulin from embryo extracts by bacterially-purified MBP-tagged N-
1158 terminal fragments of Cnn, as indicated. The blot was probed with anti-MBP and anti-γ-tubulin
1159 antibodies, as indicated. Band intensities were normalised within each experiment to the γ-
1160 tubulin band in the respective MBP-Cnn-T-N IP, as in Figure 1G. On average, the band
1161 intensities of γ-tubulin from the MBP-Cnn-C-N, MBP-Cnn-C-N^{P1}, and MBP-Cnn-C-N^{T27} IPs
1162 were ~18%, 44%, and 34%, respectively, in comparison to the average band intensity of γ-
1163 tubulin from the MBP-Cnn-T-N IP. Horizontal lines represent the mean.
1164
1165 **Figure 5**
1166 **Mis-expression of the Cnn-T N-terminus results in cell division defects. (A)** Diagram of
1167 normal Cnn-C and chimeric Cnn-C^T in which the unique N-terminus of Cnn-C (dark blue) is
1168 replaced by the unique N-terminus of Cnn-T (red). **(B)** Graph showing quantification of
1169 hatching rate of progeny from crosses of pUbq-Cnn-C or pUbq-Cnn-C^T males and females to
1170 wild-type flies, as indicated. The mean proportion of embryos that hatched is shown, and error
1171 bars show 95% confidence intervals. **(C)** Western blots of protein extracts from embryos and
1172 testes of wild-type (WT), pUbq-Cnn-C, and pUbq-Cnn-C^T flies as indicated. Blots were probed
1173 with anti-γ-tubulin, anti-Cnn-C (N-term), anti-Cnn-C (C-term), and anti-Cnn-T^N antibodies as
1174 indicated. Endogenous Cnn-C is indicated by a black arrowhead; combined endogenous and
1175 pUbq-driven Cnn-C is indicated by a blue arrowhead in the pUbq-Cnn-C lanes. Cnn-C^T is
1176 indicated by a red arrowhead; non-specific bands of approximately the same size as Cnn-C^T
1177 are marked with asterisks. **(D)** Western blot showing results of anti-Cnn immunoprecipitation
1178 from embryo extracts expressing pUbq-Cnn-C or pUbq-Cnn-C^T as indicated. Red arrowhead
1179 indicates Cnn-C^T. Note that, given the low expression of pUbq-Cnn-C^T within embryos, gel

1180 loading of the IP lanes was adjusted to try to better balance the amount of Cnn protein. **(E)**
1181 Graph showing quantification of defects in fixed embryos. Embryos were classified into
1182 categories (during a blind analysis) based on whether they were perceived to be normal, or to
1183 display severe, moderate or mild defects, based both on how widespread defects were and
1184 the severity of individual defects. **(F)** Fluorescent images show either syncytial pUbq-Cnn-C
1185 embryos (top panels) or pUbq-Cnn-C^T embryos (bottom panels) in either S-phase (left panels)
1186 or M-phase (right panels). Images were selected to show extreme examples i.e. normal S-
1187 phase and M-phase in pUbq-Cnn-C embryos and strongly perturbed S-phase, including the
1188 presence of cytosolic microtubules, and M-phase in pUbq-Cnn-C^T embryos. **(G)** Phase
1189 contrast images showing round spermatids from testes of flies expressing pUbq-Cnn-C or
1190 pUbq-Cnn-C^T. Alterations in nucleus: nebenkern ratio (normally 1:1, asterisks in right panel)
1191 and size (normally approximately equal) indicate defects in cytokinesis and karyokinesis. **(H)**
1192 Graph showing quantification of the nucleus:nebenkern ratio (left panel) and variance in
1193 nuclear diameter (right panel) in pUbq-Cnn-C and pUbq-Cnn-C^T testes. Error bars show
1194 standard error of the mean. **(I)** Fluorescence images showing cytokinesis and karyokinesis
1195 defects during meiosis in pUbq-Cnn-C^T testes. Microtubules (green, α-tubulin), centrosomes
1196 (pink, Asterless), and DNA (blue) are marked. Cytosolic microtubules not associated with
1197 centrosomes can be observed (arrows), suggesting ectopic cytosolic microtubule nucleation.
1198

1199 # Supplementary Figure Legends

1200

1201 **Figure S1**

1202 **Diagrams of different Cnn constructs (omitting the tags) used in this study. (A)** Diagram
1203 showing full-length Cnn constructs without modifications to the PReM domain. Cnn-C is the
1204 major centrosomal isoform in *Drosophila*. Cnn-T is the testes-specific isoform in *Drosophila*.
1205 Cnn-C^T represents an artificial form of Cnn-C in which the N-terminal region of Cnn-C (dark
1206 blue) has been replaced with the N-terminal region of Cnn-T (red). **(B)** Diagram showing Cnn
1207 constructs containing phospho-mimetic mutations in their PReM domain to drive scaffold
1208 formation *in vivo*. The constructs differ only in their N-termini: Cnn-C-$PReM^m$ and Cnn-C^T-
1209 $PReM^m$ each contain the Cnn-C or Cnn-T unique N-terminal region, respectively. Cnn-$C^{\Delta 1\text{-}77}$-
1210 $PReM^m$ is a version of Cnn-C lacking its specific N-terminal extension region (the CAI domain).
1211 **(C)** Diagram showing bacterially-purified N-terminal fragments of different Cnn types. Each
1212 fragment contains the CM1 domain (purple); in addition, Cnn-C-N and Cnn-T-N contain unique
1213 N-terminal regions (dark blue and red respectively).

1214

1215 **Figure S2**

1216 **Bacterially-purified MBP-Cnn-T-N fragments immunoprecipitate γ-Tubulin Ring**
1217 **Complexes. (A)** Western blot showing results of anti-MBP immunoprecipitation from embryo
1218 extracts expressing GFP-tagged Grip proteins (homologues of GCP4,5,6), either
1219 supplemented (+) or not supplemented (-) with MBP-Cnn-T-N, as indicated. Blots were probed
1220 with anti-GFP, anti-Grip71 and anti-γ-tubulin antibodies as indicated. When using MBP-Cnn-
1221 T-N, γ-tubulin and Grip71, as well as Grip75, 128, or 163, are co-immunoprecipitated. **(B)**
1222 Mass spectrometry results from IPs with MBP-Cnn-T-N showing the presence of various γ-
1223 TuRC components. Note that Mzt1 is not expressed within embryos. Results of a control
1224 experiment on Grip75-GFP embryo extract not supplemented with any MBP-Cnn-T-N
1225 fragment are also shown. Numbers indicate emPAI scores as a proxy for protein abundance.
1226 Grip84 (A) and Grip84 (E) represent two different isoforms of Grip84 (promoters 1 and 2
1227 respectively).

1228

1229 **Figure S3**

1230 **Protein alignment of N-terminal regions of Cnn-C proteins from different *Drosophila***
1231 **species.** The alignment was carried out in JalView keeping *D. melanogaster* at the top with
1232 the closest related species in order below. Only the N-terminal regions of the proteins were
1233 used in the alignment (~1-255aa). Potential phosphorylation patches are highlighted in yellow,

1234 with the proportion of S/T residues present in the *Drosophila melanogaster* sequence
1235 indicated in brackets. The CM1 domain is highlighted in purple. Red boxes and green arrows
1236 indicate a-helices and β-sheets based on predictions from JPred.
1237
1238 **Figure S4**
1239 **Polarity is established normally in pUbq-Cnn-C^T oocytes. (A-B)** Fluorescent images show
1240 localisation of Staufen protein in oocytes expressing pUbq-Cnn-C (A) or pUbq-Cnn-C^T (B) at
1241 stages 8, 9 and 10, as indicated. **(C)** Fluorescent images show localisation of Gurken protein
1242 in oocytes expressing pUbq-Cnn-C or pUbq-Cnn-C^T at stage 9. Localisation of Staufen and
1243 Gurken are not perturbed in oocytes expressing pUbq-Cnn-C^T indicating that there are no
1244 major defects in microtubule organisation.
1245
1246 **Figure S5**
1247 **Major spermatocyte defects are observed within testes from pUbq-Cnn-C^T flies**
1248 Fluorescence images showing cytokinesis and karyokinesis defects during meiosis in pUbq-
1249 Cnn-C^T testes. Microtubules (green, γ-tubulin), centrosomes (pink, Asterless), and DNA (blue)
1250 are marked.
1251

1252 Supplementary Videos

1253 **Video 1**
1254 **Cnn-T scaffolds organise microtubule asters and can be mobile.** Movie showing Cnn-T
1255 scaffolds (green) organising microtubule asters (marked with Jupiter-mCherry (magenta)). A
1256 mobile scaffold (lower left) with an asymmetric microtubule aster can be seen moving through
1257 the cytosol.
1258
1259 **Video 2**
1260 **Transient spindle-like structures can form between Cnn scaffolds.** Movie showing the
1261 formation and disappearance of a transient spindle-like structure between adjacent Cnn-T
1262 scaffolds (green). Microtubules are marked with Jupiter-mCherry (magenta).
1263
1264 **Video 3**
1265 **Spindle-like structures organised by Cnn scaffolds can form in synchrony.** Movie
1266 showing the synchronous formation and disappearance of a multi-polar spindle-like array of
1267 microtubules that is subsequently organised by a nearby group of coalescing Cnn scaffolds
1268 (green). Microtubules are marked with Jupiter-mCherry (magenta)

1269

1270 **Video 4**

1271 **Microtubules are robustly anchored to Cnn scaffolds.** Movie showing rare giant Cnn-T
1272 scaffolds (green). One scaffold can be seen rotating and dragging the microtubules, indicating
1273 that the microtubules are robustly attached to the scaffold, presumably via γ-TuRCs.
1274 Microtubules are marked with Jupiter-mCherry (magenta).

1275

1276 **Video 5**

1277 **Expression of GFP-Cnn-T-N leads to the formation of dynamic microtubules within the**
1278 **cytosol of unfertilised eggs.** Left panel shows a movie displaying dynamic cytoplasmic
1279 microtubules formed upon injection of mRNA encoding GFP-Cnn-T-N into unfertilised eggs.
1280 Right panel shows a movie of an unfertilised egg injected with water alone (control).
1281 Microtubules are marked with Jupiter-mCherry (magenta).

1282

Figure 1

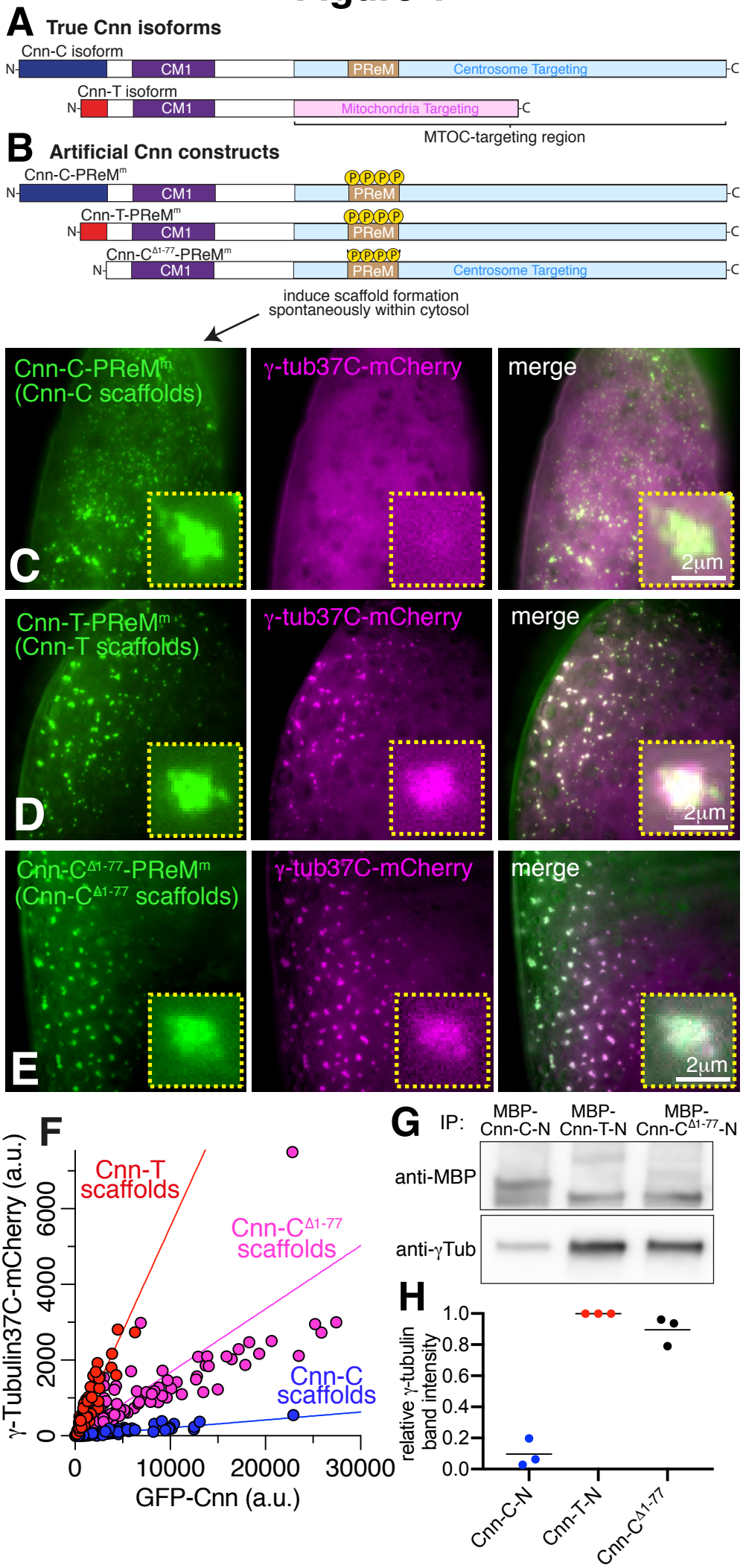
A True Cnn isoforms
Cnn-C isoform
N-
CM1
PReM
Centrosome Targeting
-C
Cnn-T isoform
N-
CM1
Mitochondria Targeting
-C
MTOC-targeting region
B Artificial Cnn constructs
Cnn-C-PReM^m
P P P P
PReM
Cnn-T-PReM^m
Cnn-C^Δ1-77-PReM^m
induce scaffold formation
spontaneously within cytosol
Cnn-C-PReM^m
(Cnn-C scaffolds)
γ-tub37C-mCherry
merge
C
2μm
Cnn-T-PReM^m
(Cnn-T scaffolds)
D
Cnn-C^Δ1-77-PReM^m
(Cnn-C^Δ1-77 scaffolds)
E
F
Cnn-T scaffolds
Cnn-C^Δ1-77 scaffolds
Cnn-C scaffolds
γ-Tubulin37C-mCherry (a.u.)
GFP-Cnn (a.u.)
0
2000
4000
6000
10000
20000
30000
G
IP:
MBP-Cnn-C-N
MBP-Cnn-T-N
MBP-Cnn-C^Δ1-77-N
anti-MBP
anti-γTub
H
relative γ-tubulin band intensity
1.0
0.8
0.6
0.4
0.2
0.0
Cnn-C-N
Cnn-T-N
Cnn-C^Δ1-77

Figure 2

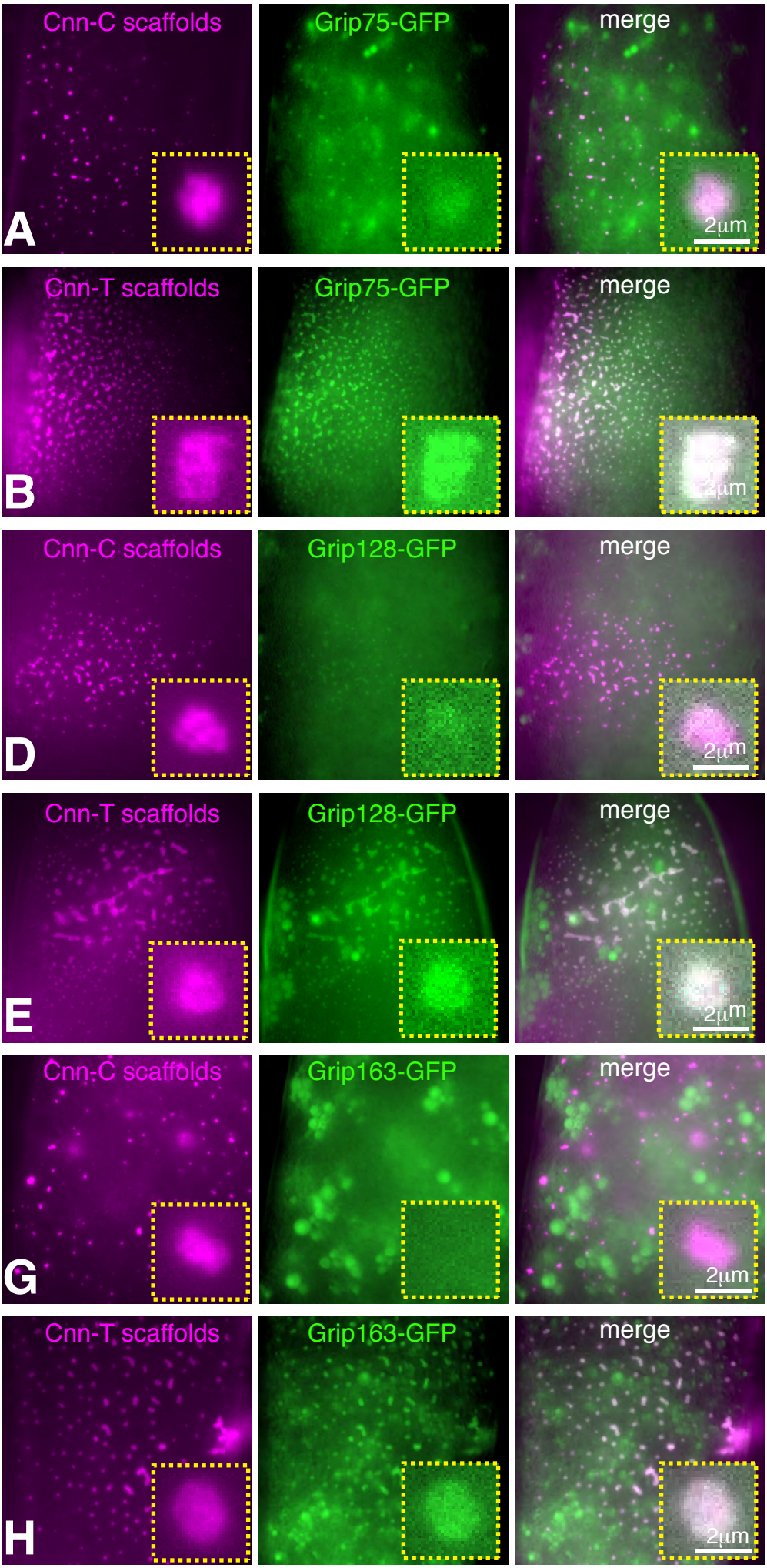
Cnn-C scaffolds
Grip75-GFP
merge
A
2μm
Cnn-T scaffolds
Grip75-GFP
merge
B
2μm
Cnn-C scaffolds
Grip128-GFP
merge
D
2μm
Cnn-T scaffolds
Grip128-GFP
merge
E
2μm
Cnn-C scaffolds
Grip163-GFP
merge
G
2μm
Cnn-T scaffolds
Grip163-GFP
merge
H
2μm

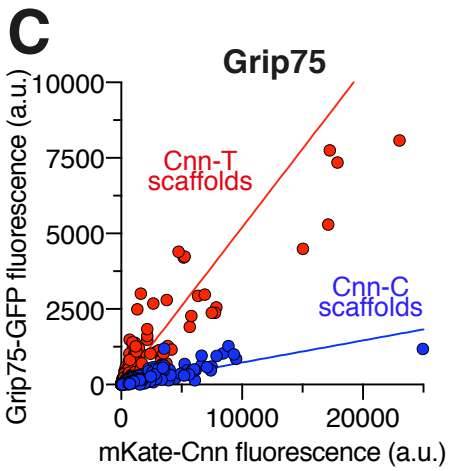
C
Grip75
Grip75-GFP fluorescence (a.u.)
10000
7500
5000
2500
0
Cnn-T scaffolds
Cnn-C scaffolds
0
10000
20000
mKate-Cnn fluorescence (a.u.)

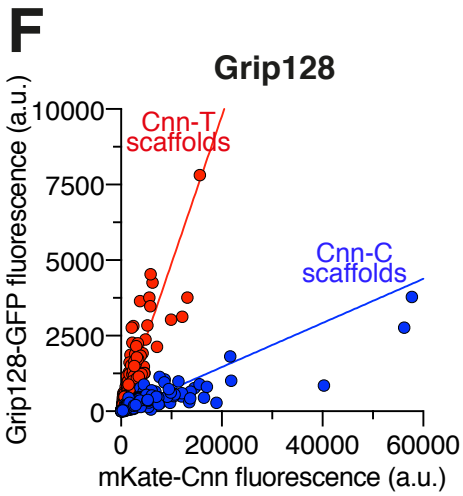
F
Grip128
Grip128-GFP fluorescence (a.u.)
10000
7500
5000
2500
0
Cnn-T scaffolds
Cnn-C scaffolds
0
20000
40000
60000
mKate-Cnn fluorescence (a.u.)

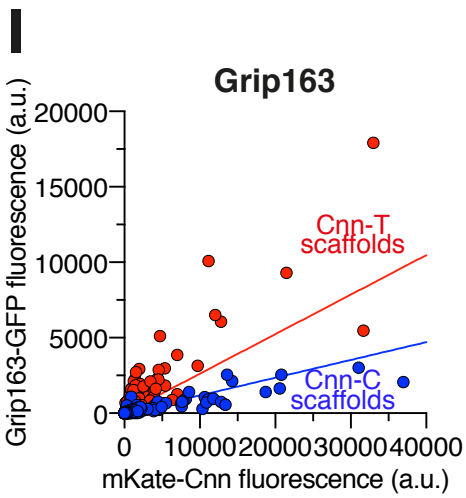
I
Grip163
Grip163-GFP fluorescence (a.u.)
20000
15000
10000
5000
0
Cnn-T scaffolds
Cnn-C scaffolds
0
10000
20000
30000
40000
mKate-Cnn fluorescence (a.u.)

Figure 3

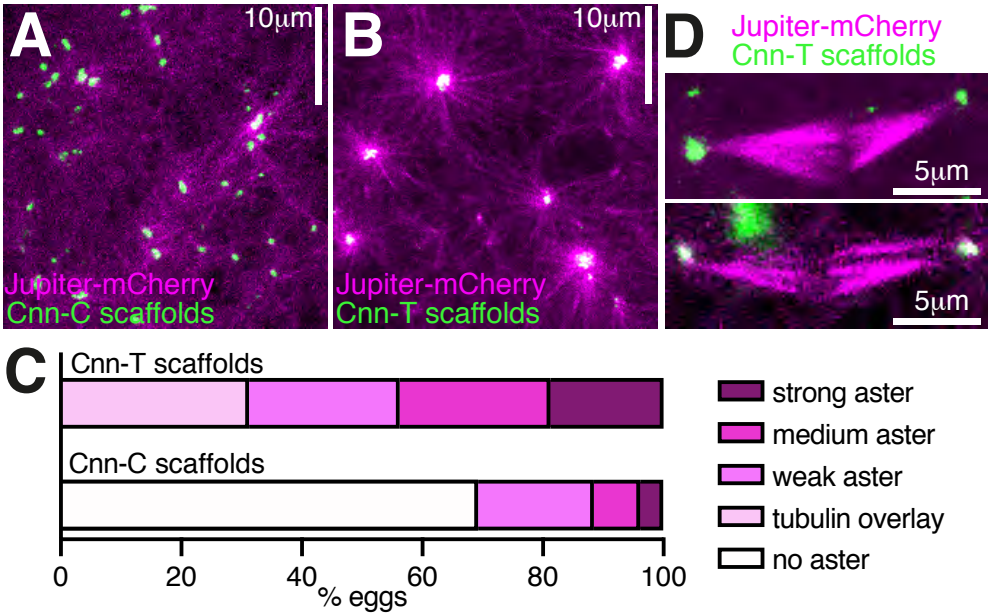
A
10μm
Jupiter-mCherry
Cnn-C scaffolds
B
10μm
Jupiter-mCherry
Cnn-T scaffolds
D
Jupiter-mCherry
Cnn-T scaffolds
5μm
5μm
C
Cnn-T scaffolds
Cnn-C scaffolds
0
20
40
60
80
100
% eggs
strong aster
medium aster
weak aster
tubulin overlay
no aster

Figure 4

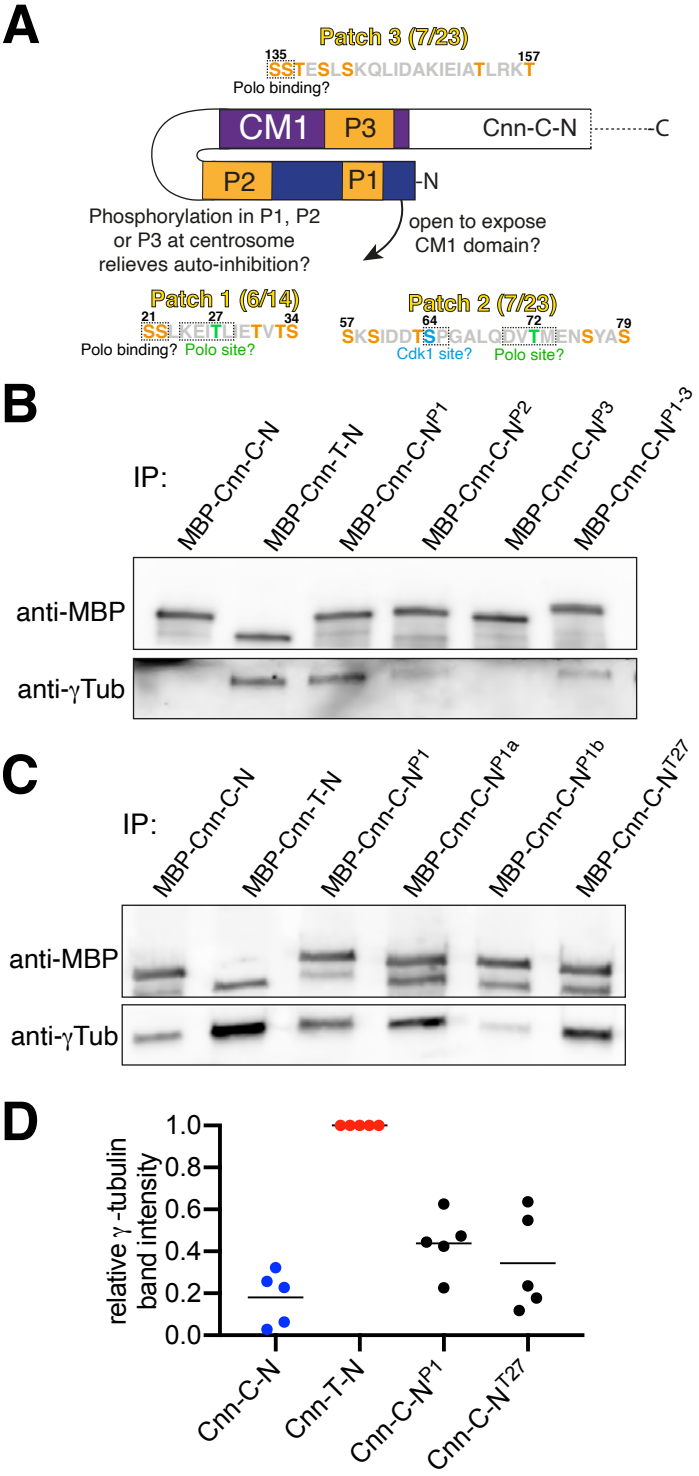
A
Patch 3 (7/23)
135
157
Polo binding?
CM1
P3
Cnn-C-N
C
P2
P1
N
Phosphorylation in P1, P2 or P3 at centrosome relieves auto-inhibition?
open to expose CM1 domain?
Patch 1 (6/14)
21
27
34
Polo binding?
Polo site?
Patch 2 (7/23)
57
64
72
79
Cdk1 site?
Polo site?
B
IP:
MBP-Cnn-C-N
MBP-Cnn-T-N
MBP-Cnn-C-N^{P1}
MBP-Cnn-C-N^{P2}
MBP-Cnn-C-N^{P3}
MBP-Cnn-C-N^{P1-3}
anti-MBP
anti-γTub
C
IP:
MBP-Cnn-C-N
MBP-Cnn-T-N
MBP-Cnn-C-N^{P1}
MBP-Cnn-C-N^{P1a}
MBP-Cnn-C-N^{P1b}
MBP-Cnn-C-N^{T27}
anti-MBP
anti-γTub
D
relative γ-tubulin band intensity
1.0
0.8
0.6
0.4
0.2
0.0
Cnn-C-N
Cnn-T-N
Cnn-C-N^{P1}
Cnn-C-N^{T27}

Figure 5

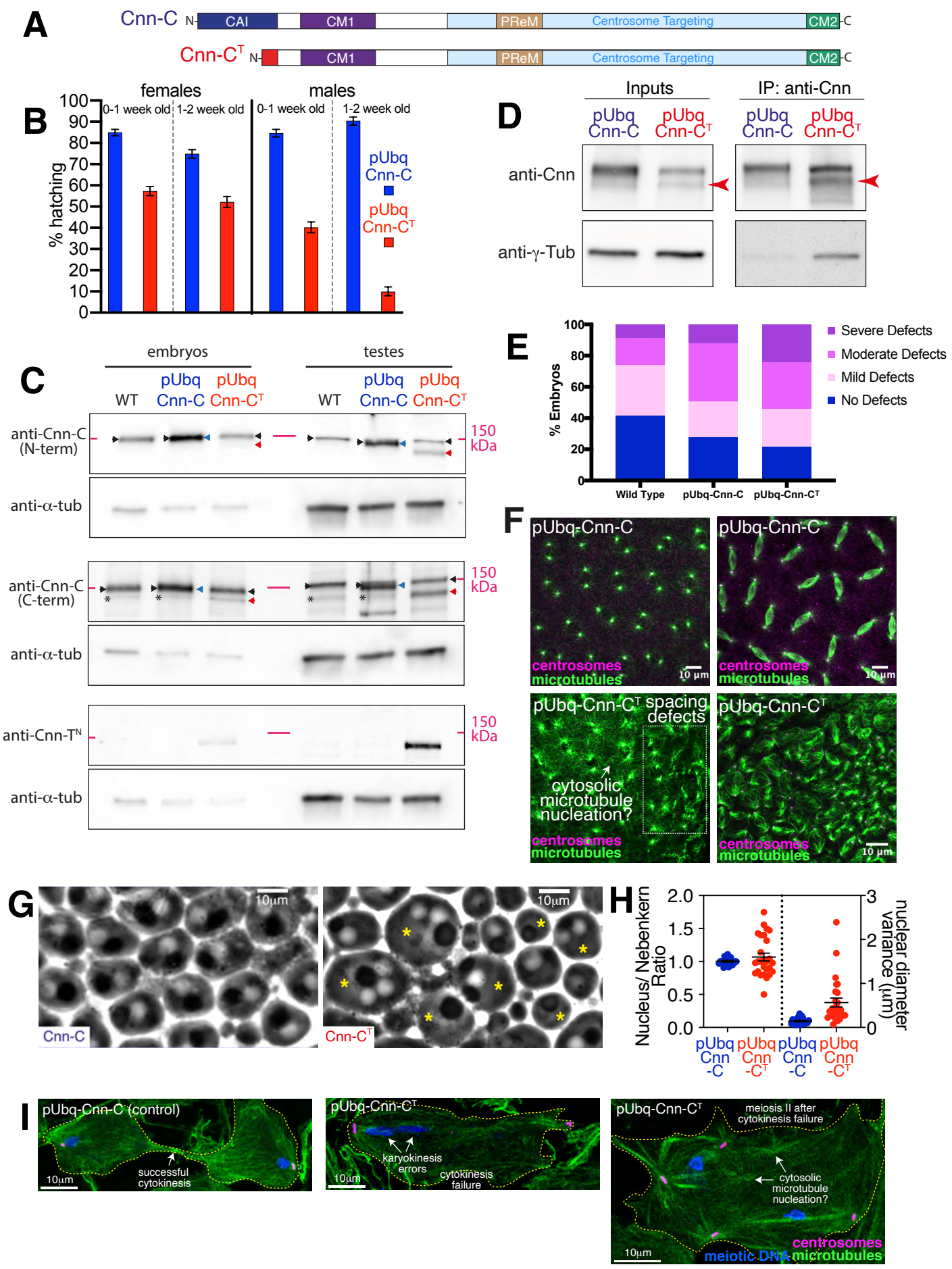
A
Cnn-C
N-
CAI
CM1
PReM
Centrosome Targeting
CM2
-C
Cnn-C^T
B
females
males
0-1 week old
1-2 week old
% hatching
pUbq Cnn-C
pUbq Cnn-C^T
C
embryos
testes
WT
anti-Cnn-C (N-term)
anti-α-tub
anti-Cnn-C (C-term)
anti-Cnn-T^N
150 kDa
D
Inputs
IP: anti-Cnn
anti-Cnn
anti-γ-Tub
E
% Embryos
Severe Defects
Moderate Defects
Mild Defects
No Defects
Wild Type
pUbq-Cnn-C
pUbq-Cnn-C^T
F
pUbq-Cnn-C
centrosomes
microtubules
10 µm
pUbq-Cnn-C^T
spacing defects
cytosolic microtubule nucleation?
G
10µm
Cnn-C
Cnn-C^T
H
Nucleus/ Nebenkern Ratio
nuclear diameter variance (µm)
I
pUbq-Cnn-C (control)
successful cytokinesis
karyokinesis errors
cytokinesis failure
meiosis II after cytokinesis failure
cytosolic microtubule nucleation?
meiotic DNA

Figure S1

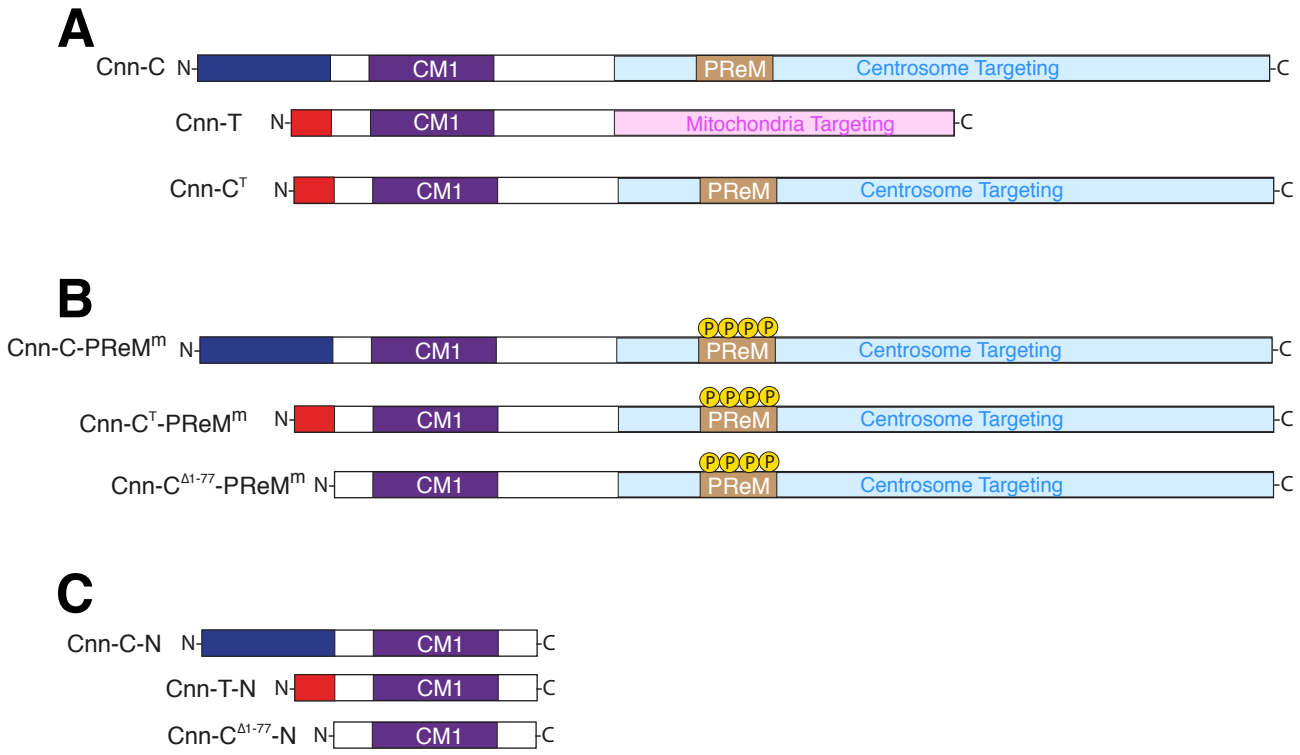
A
Cnn-C
N-
CM1
PReM
Centrosome Targeting
-C
Cnn-T
N-
CM1
Mitochondria Targeting
-C
Cnn-C^{T}
N-
CM1
PReM
Centrosome Targeting
-C
B
Cnn-C-PReM^{m}
N-
CM1
P P P P
PReM
Centrosome Targeting
-C
Cnn-C^{T}-PReM^{m}
N-
CM1
P P P P
PReM
Centrosome Targeting
-C
Cnn-C$^{\Delta 1\text{-}77}$-PReM^{m}
N-
CM1
P P P P
PReM
Centrosome Targeting
-C
C
Cnn-C-N
N-
CM1
-C
Cnn-T-N
N-
CM1
-C
Cnn-C$^{\Delta 1\text{-}77}$-N
N-
CM1
-C

Figure S2

A

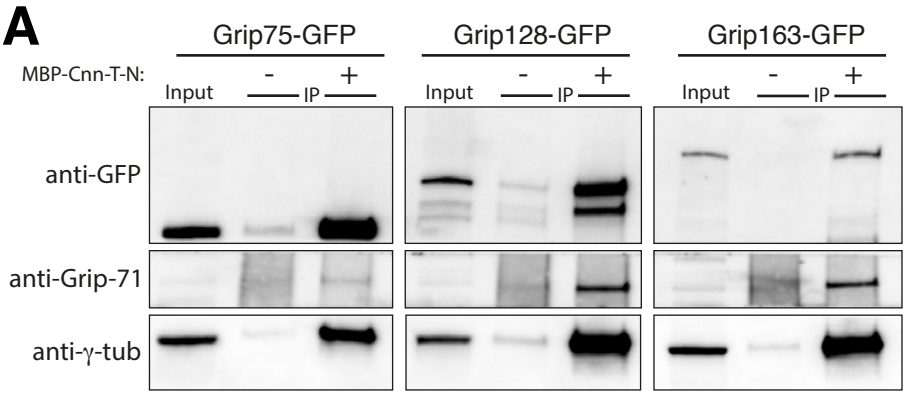

B

UniProt entry	Protein	G75, no fragment	G75 + Cnn-T-N	G128 + Cnn-T-N	G163 + Cnn-T-N
A0A0B4K6Z9	**Cnn**	-	4.50	15.63	13.03
M9PDN9	**ytubulin 37C**	0.45	24.45	63.16	39.41
P23257	**ytubulin 23C**	-	1.04	1.90	1.43
E1JJQ3	**Grip 84**	-	1.76	8.14	4.76
Q8IQW7	**Grip 84**	-	1.54	7.44	-
Q9XYP8	**Grip 91**	-	1.74	4.45	3.54
Q9VKU7	**Grip 75**	0.07	0.88	3.57	2.54
Q9VXU8	**Grip 128**	-	0.08	0.40	0.16
Q9VTS3	**Grip 163**	-	0.24	1.09	0.24
Q9VJ57	**Grip71**	-	0.30	1.87	0.93
X2JCP8	**Actin**	40.63	17.87	22.66	32.21

Figure S3

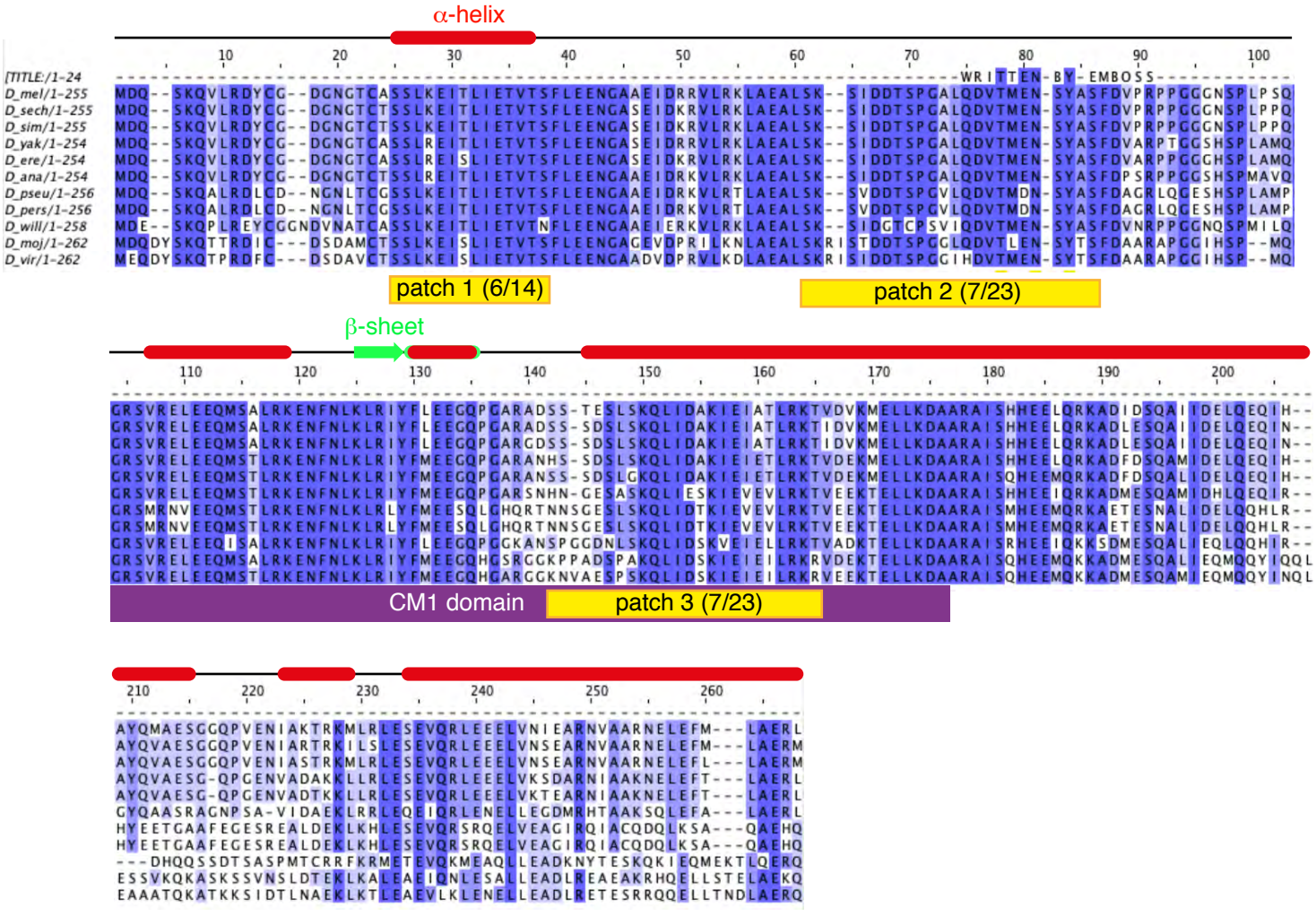
α-helix
10 20 30 40 50 60 70 80 90 100
[TITLE:/1-24
D_mel/1-255
D_sech/1-255
D_sim/1-255
D_yak/1-254
D_ere/1-254
D_ana/1-254
D_pseu/1-256
D_pers/1-256
D_will/1-258
D_moj/1-262
D_vir/1-262
patch 1 (6/14)
patch 2 (7/23)
β-sheet
110 120 130 140 150 160 170 180 190 200
CM1 domain
patch 3 (7/23)
210 220 230 240 250 260

Figure S4

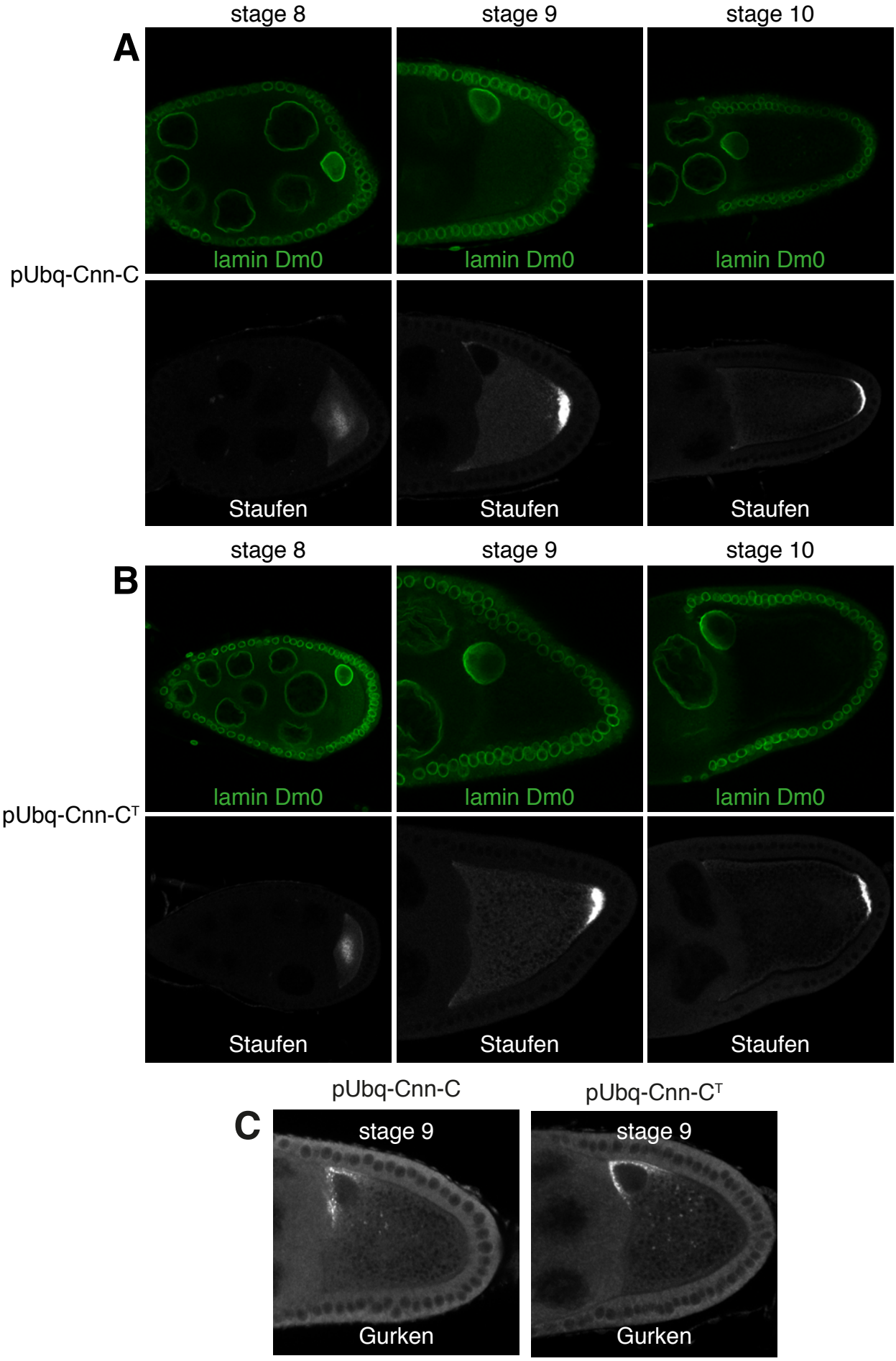
A
stage 8
stage 9
stage 10
pUbq-Cnn-C
lamin Dm0
lamin Dm0
lamin Dm0
Staufen
Staufen
Staufen
B
stage 8
stage 9
stage 10
pUbq-Cnn-C^{T}
lamin Dm0
lamin Dm0
lamin Dm0
Staufen
Staufen
Staufen
C
pUbq-Cnn-C
pUbq-Cnn-C^{T}
stage 9
stage 9
Gurken
Gurken

Figure S5

examples of spermatocytes within testes of pUbq-Cnn-C^{T} flies
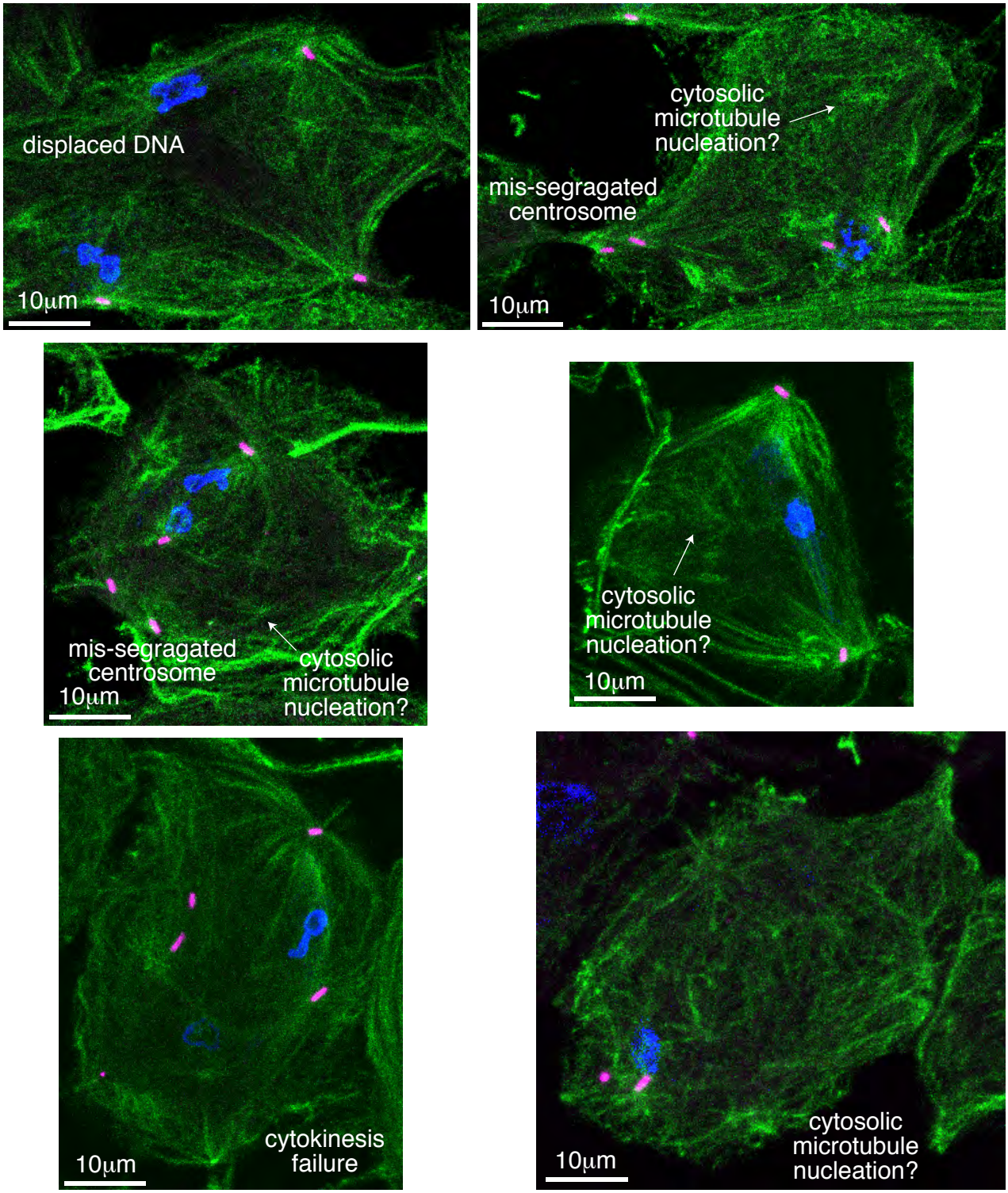
meiotic DNA
centrosomes
microtubules